THE JOURNAL OF CHEMICAL PHYSICS **143**, 244305 (2015)

Infrared laser induced population transfer and parity selection in $^{14}NH_3$: A proof of principle experiment towards detecting parity violation in chiral molecules

P. Dietiker, E. Miloglyadov, M. Quack,[a] A. Schneider, and G. Seyfang
Physical Chemistry, ETH Zürich, CH-8093 Zürich, Switzerland

(Received 6 August 2015; accepted 18 November 2015; published online 23 December 2015)

We have set up an experiment for the efficient population transfer by a sequential two photon—absorption and stimulated emission—process in a molecular beam to prepare quantum states of well defined parity and their subsequent sensitive detection. This provides a proof of principle for an experiment which would allow for parity selection and measurement of the time evolution of parity in chiral molecules, resulting in a measurement of the parity violating energy difference $\Delta_{pv}E$ between enantiomers of chiral molecules. Here, we present first results on a simple achiral molecule demonstrating efficient population transfer (about 80% on the average for each step) and unperturbed persistence of a selected excited parity level over flight times of about 1.3 ms in the beam. In agreement with model calculations with and without including nuclear hyperfine structure, efficient population transfer can be achieved by a rather simple implementation of the rapid adiabatic passage method of Reuss and coworkers and considering also the stimulated Raman adiabatic passage technique of Bergmann and coworkers as an alternative. The preparation step uses two powerful single mode continuous wave optical parametric oscillators of high frequency stability and accuracy. The detection uses a sensitive resonantly enhanced multiphoton ionization method after free flight lengths of up to 0.8 m in the molecular beam. Using this technique, we were able to also resolve the nuclear hyperfine structure in the rovibrational levels of the ν_1 and ν_3 fundamentals as well as the $2\nu_4$ overtone of $^{14}NH_3$, for which no previous data with hyperfine resolution were available. We present our new results on the quadrupole coupling constants for the ν_1, ν_3, and $2\nu_4$ levels in the context of previously known data for ν_2 and its overtone, as well as ν_4, and the ground state. Thus, now, ^{14}N quadrupole coupling constants for all fundamentals and some overtones of $^{14}NH_3$ are known and can be used for further theoretical analysis. © *2015 AIP Publishing LLC*. [http://dx.doi.org/10.1063/1.4936912]

I. INTRODUCTION

Molecular chirality is a central concept of stereochemistry and has a long history in chemical research.[1–7] Molecular chirality is also related to fundamental physics through the underlying symmetries of physical laws[8] and to biological evolution in relation to the origin of biomolecular homochirality.[6–13] Indeed, with space inversion symmetry and parity conservation, the reaction enthalpy for the stereomutation reaction (1) converting the *R*-enantiomer of a chiral molecule into the *S*-enantiomer,

$$R \rightleftharpoons S, \qquad \Delta_R H_0^{\ominus}(1) = ?, \qquad (1)$$

would be exactly zero by symmetry, the ground state energies (and also all corresponding excited energy levels) being exactly identical for the enantiomers by symmetry.[1–8] The situation has changed fundamentally with the discovery of parity violation.[14–22] In this case, one predicts a small "parity violating" energy difference $\Delta_{pv}E_0$ for the ground state energies of the enantiomers, corresponding to a nonzero value of the reaction enthalpy (N_A being the Avogadro constant),

$$\Delta_R H_0^{\ominus}(1) = \Delta_{pv} H_0^{\ominus} = N_A \Delta_{pv} E_0. \qquad (2)$$

While qualitative and semiquantitative estimates for $\Delta_{pv}E_0$ have existed for quite some time[23–27] and parity violating effects have been well proven in atomic spectroscopy,[28–33] so far no experiment to measure $\Delta_{pv}E_0$ or related quantities in chiral molecules has been successful, because of the very small magnitude predicted for such effects. However, compared to the early theoretical estimates,[23–27] the more recent theoretical developments have led to substantial increase in the predicted $\Delta_{pv}E$, by a factor of 100 for the benchmark molecule H_2O_2 and typically by one to two orders of magnitude also for other molecules[34–44] (see also the reviews of Refs. 8, 13, and 45–50). This has favourably changed the outlook of doing successful experiments. Typical values derived for CHFClBr, as an example, are about $\Delta_{pv}H_0^{\ominus} = 10^{-11}$ J/mol.[40–42]

While quite a few experimental schemes have been proposed to measure parity violation in chiral molecules (see Refs. 51–56, for example, and the reviews of Refs. 8, 11, 13, and 48–50 for a more complete survey), at present only two basic experimental, spectroscopic schemes appear to be seriously pursued, as outlined schematically in Figure 1.

[a]Author to whom correspondence should be addressed. Electronic mail: Martin@Quack.ch. Telephone: ++41-44-6324421. Fax: ++41-44-6321021.

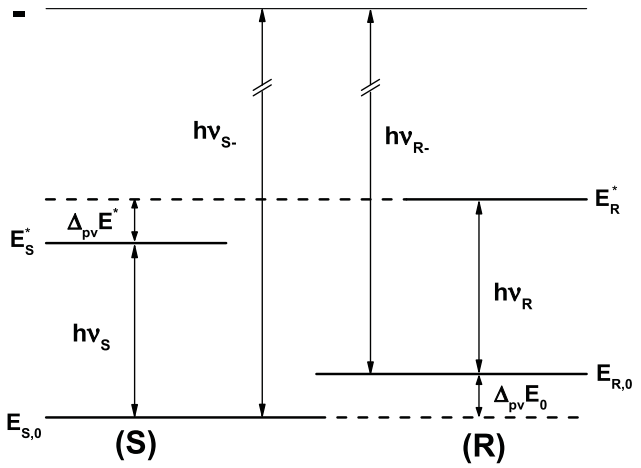

FIG. 1. Scheme of energy levels and spectroscopic experiments for parity-violating energy differences $\Delta_{\rm pv}E$. One notes that in this scheme, $\Delta\nu_{\rm pv} = \nu_{\rm R} - \nu_{\rm S} = (\Delta_{\rm pv}E^* - \Delta_{\rm pv}E_0)/h$. $\Delta_{\rm pv}E_0$ and $\Delta_{\rm pv}E^*$ are the expectation values of the parity violating potential energy difference for the respective rovibrational quantum states (see Refs. 8, 13, and 44 and text).

In the first scheme, originally proposed by Letokhov and coworkers,[25,51] one measures the difference of line positions, say in the infrared spectrum of the separated enantiomers ($(h\nu_{\rm R} - h\nu_{\rm S})$ in Figure 1). This results in a difference of parity violating energy differences $(\Delta_{\rm pv}E^* - \Delta_{\rm pv}E_0)$ in two different energy levels. For CHFClBr, spectroscopic experiments were carried out by Kompanets *et al.*[51] and this work was pursued later by us with more precise rovibrational analyses in molecular beam experiments towards identifying suitable lines for detecting parity violation in CHFClBr spectra,[57] which were then used to carry out experiments at very high precision.[58] We refer to Refs. 59 and 60 for the current status of such attempts in two other groups currently active along these lines, which we shall not discuss further here.

In the second scheme, proposed in Refs. 54 and 55, one uses an excited intermediate level of well defined parity (say, negative parity marked by – in Fig. 1) to measure directly $\Delta_{\rm pv}E_0$ (or some $\Delta_{\rm pv}E^*$) separately. This can be done either in a frequency resolved experiment by measuring the corresponding combination difference[55] or in a time resolved experiment by preparing a time dependent state of well defined initial parity, which evolves in time and where, thus, $\Delta_{\rm pv}E$ can be derived from this time dependence, which can in principle be measured by a highly sensitive spectroscopic detection of parity on the millisecond time scale.

It is the aim of the present paper to present an experimental setup and a proof of principle experiment on the achiral molecule ammonia ($^{14}NH_3$), for which we also derive some new and highly precise spectroscopic results using this setup. A preliminary account of the present work has been given in Ref. 61.

Figure 2 shows a more detailed scheme for the potential functions, energy levels, and wavefunctions relevant for the time resolved experiment to measure parity violation in a chiral molecule and also, in a different limit of the experiment, for ammonia NH_3 (or NHDT, which would be chiral at the equilibrium geometry). As discussed elsewhere in detail,[8,13,44] electro-weak parity violation introduces a multidimensional parity violating potential hypersurface $V_{pv}^{el}(q)$. For a chiral isotopomer or molecule, one can calculate a purely electronic parity violating energy difference $\Delta_{pv}E_{el}$ arising from the difference of these potentials at the equilibrium geometry of the enantiomers. However, for NHDT, where the ground state tunneling splitting $\Delta E_{\pm}$ for the symmetrical potential without parity violation is much larger than the parity violating energy difference $\Delta_{\rm pv}E_{\rm el}$ arising from the slightly asymmetric effective potential due to parity violation,[44]

$$\Delta E_{\pm} \gg \Delta_{\rm pv}E_{\rm el}, \tag{3}$$

one has delocalized tunneling energy eigenstates of well defined parity (+ or –), χ_+ and χ_- in a double well potential, which can be described by a superposition of left localized and right localized states,

$$\chi_+ = \frac{1}{\sqrt{2}}(\lambda + \rho), \tag{4}$$

$$-\chi_- = \frac{1}{\sqrt{2}}(\lambda - \rho), \tag{5}$$

with eigenstate energies E_+ and E_- separated by $\Delta E_{\pm} = E_- - E_+$. As is well known, tunneling of localized wave functions, λ and ρ will occur with a period $\tau = h/\Delta E_{\pm}$,[4,5]

$$\lambda = \frac{1}{\sqrt{2}}(\chi_+ - \chi_-), \tag{6}$$

$$\rho = \frac{1}{\sqrt{2}}(\chi_+ + \chi_-). \tag{7}$$

However, for stable chiral molecules in the electronic ground state, where parity violation dominates the quantum dynamics,[48] and thus, $\Delta_{\rm pv}E$ is much larger than the tunneling splitting $\Delta E_{\pm}$ for the symmetrical case, one has

$$\Delta_{\rm pv}E \gg \Delta E_{\pm}, \tag{8}$$

and thus, the energy eigenfunctions are the localized functions λ (with eigenenergy E_S) and ρ (with eigenenergy E_R) separated by $\Delta_{\rm pv}E = E_R - E_S$ (see Figure 1, we use the notation $\Delta_{\rm pv}E$, when indicating some general level, not necessarily the ground state). If one prepares an initial state with well defined parity (say χ_+ at $t = 0$), the time dependent wave function $\Psi(t)$ will show a time evolution of parity according to

$$\Psi(t) = \frac{1}{\sqrt{2}}\exp(-iE_\lambda t/\hbar)[\lambda + \rho\exp(-i\Delta_{\rm pv}Et/\hbar)]. \tag{9}$$

The probability of finding a given parity $p^+(t)$ (for positive parity) or $p^-(t)$ (for negative parity) is given by

$$p^-(t) = 1 - p^+(t) = \sin^2(\pi\Delta_{\rm pv}Et/h). \tag{10}$$

These probabilities can be measured with high sensitivity, for instance, with REMPI detection (by resonantly enhanced multiphoton ionization) using (for example) an achiral excited electronic state (planar in Figure 2), where the absorption lines corresponding to strongly allowed electric dipole transitions to positive and negative parity states are well separated (with separation on the order of MHz, corresponding to rovibrational line separations, depending on the molecule).

The examples shown in Figure 2 correspond to a two step preparation of a state of well defined positive initial

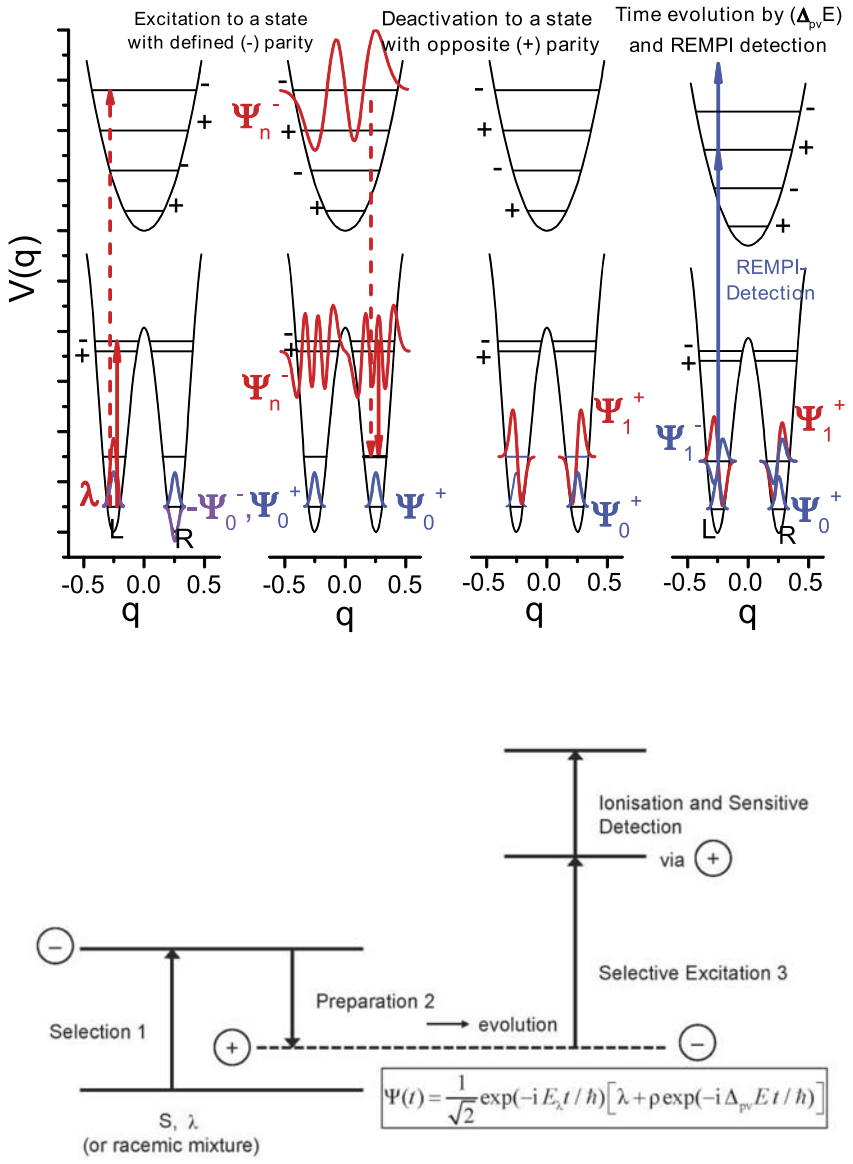

FIG. 2. Upper part: scheme of the preparation and detection steps for the time resolved experiment to measure $\Delta_{pv}E$. The transitions to the intermediate states are indicated together with the corresponding wave functions for an excited state with the well defined parity close to the barrier of a double minimum potential (full line) or an achiral electronically excited state (dashed line) as an intermediate. The right hand part shows the sensitive detection step with REMPI. Lower part: sequence of steps in the experiment on molecular parity violation.

parity with an intermediate excited state of negative parity. This preparation can make use of absorption to an achiral excited electronic state and subsequent stimulated emission (dashed arrows in Figure 2), as, for instance, in a molecule like difluoroallene,[62] which is chiral in the ground state and achiral, quasiplanar in the excited state (using typically two UV-photons). Alternatively, one can use as intermediate state levels near or above the barrier in the electronic ground state, which have well defined parity, if condition (3) is satisfied (for example, in a molecule like ClOOCl[63]). Then, one might use two infrared photons (full lines in the left hand part in Figure 2). The scheme with two infrared photons is also applicable for NH_3, where the states of well defined parity will be stationary states, and thus, parity shows no time evolution in the absence of external perturbations (collisions or external fields) as will be shown below to be the case in our test experiments, which can also be considered as tests relevant to probe the role of such external perturbations. The lower part of Figure 2 provides a simple, more schematic summary of the experiment consisting of the two step parity selection and preparation ($R,S \rightarrow \ominus \rightarrow \oplus$), evolution ($\oplus \rightarrow \ominus$) and finally selective excitation ($\ominus \rightarrow \oplus$) and sensitive detection in a third step. We shall demonstrate here all steps under realistic conditions for $^{14}NH_3$, where the initial state corresponds to a thermal mixture of parity states and the scheme leads to parity selection in the excited ensemble, which is not initially populated thermally. Of course, in the "cold" low energy ensemble, the initial almost 50:50 mixture of parity levels remains essentially unchanged. Obviously, for an achiral molecule, there is no time evolution visible due to parity violation. In this case, we prove the absence of significant perturbing effects on the selected parity level and we can use the experimental setup also to obtain new spectroscopic results on the hyperfine structure of excited vibrational levels in NH_3. In Secs. II–VI, we describe the experimental setup in detail (Section II), then describe the high resolution spectroscopy and notation for the prototype molecule NH_3 (Section III) followed by a description of methods and results for population transfer experiments (Sections IV and V), and finally provide high resolution results on the hyperfine spectra of NH_3 (Section VI).

II. EXPERIMENTAL

There are a number of conditions which have to be fulfilled in our experiments: The line widths of the lasers for the preparation step have to be small enough to obtain the required selectivity and the intensities high enough to allow for a nearly complete population transfer to the desired molecular state. After preparation, the molecular states have to be free from external perturbations for the required evolution time in the millisecond range. In our current setup, we use a molecular beam with a long enough flight path of up to 0.8 m. Finally, the detection method has to be sensitive enough to be able to detect very small amounts of the molecules with the probed parity. We shall show these conditions to be satisfied in our proof of principle experiment.

The proposed experiment to measure the parity violating energy difference $\Delta_{pv}E$ in chiral molecules by the time resolved method can be subdivided into three steps: the population of a molecular level with defined parity at modest excitation energies, which are initially not populated, through a sequential absorption and stimulated emission process; the interaction free evolution period and the sensitive detection of the population transferred to the molecular state with the opposite parity (by $\Delta_{pv}E$ if applicable, or by collisions, if these are important). The required free evolution period is determined by the magnitude of $\Delta_{pv}E$ and the sensitivity of the detection method, as the fraction of molecules transferred to the state with opposite parity may be calculated from $\Delta p = \Delta_{pv}E\ \tau_{ev}^2/\hbar$, where τ_{ev} is the evolution time between preparation and detection. For a parity violating energy difference of $\Delta_{pv}E/hc = 10^{-12}$ cm^{-1} and an evolution time of 1.3 ms, the fraction of molecules transferred to the state with opposite parity is $1.58 \cdot 10^{-6}$. Two or even more narrow bandwidth and highly frequency stable continuous wave lasers are used for the preparation step. To minimize any perturbation of the prepared molecules during the evolution period, the experiments are realized in a molecular beam setup. The sensitive detection is realized by REMPI in a time-of-flight (TOF) mass spectrometer which allows in principle for single ion detection. A schematic block diagram of the setup is shown in Figure 3 and an elevation design of the molecular beam setup is shown in Figure 4.

A. IR-laser for the preparation step

In the preparation step of the experiment, where the molecules are transferred to a state with well defined parity, two continuous wave single mode infrared optical parametric oscillators (IR-OPOs, OS4600 and Kilo, QIOPTIQ) are used. OS4600 and Kilo are singly resonant (SRO, resonant signal wave) continuous wave optical parametric oscillators which are pumped at 1.06 μm by a Nd-YAG-laser (Mephisto MOPA 18 W and 20 W, respectively, Innolight). To reduce intensity fluctuations of the OPO output, the pump laser is equipped with an active intensity noise reduction system ("noise eater") and an intensity noise $\leq$0.006% (detection bandwidth 10 Hz–2 MHz) is specified. The periodically poled MgO doped $LiNbO_3$ crystal (MgO:PPLN, periodically poled Lithium Niobate) of the OS4600 allows to cover a tuning range from 2150 to 4380 cm^{-1} for the idler radiation and from 5000 to 7250 cm^{-1} for the signal radiation with 18 different poling periods. In consequence of the Z-folded resonator design (longitudinal mode separation: 450 MHz), the idler radiation is available from two and the signal radiation from three different output ports with a total power of greater than 1 W for each spectral range. For the Kilo OPO, the poling periods of the PPLN crystal are arranged in a fan like structure allowing for a continuous tuning of the laser frequency. From the ring cavity (longitudinal mode separation: 350 MHz), an output power of up to 1.5 W for the idler wave and up to 1 W for the signal wave is available. For a selected poling period, frequency tuning of the OPO radiation is possible by changing the temperature of the PPLN crystal or through frequency tuning of the pump laser. For the Nd-YAG lasers, a frequency tuning of 30 GHz is possible on 6–8 different longitudinal modes. To increase the mode jump free tuning range of the idler radiation, an intracavity etalon is inserted in the resonator of both OPOs. However, changing the tilt angle of the etalon would result in an offset of the beam direction. To avoid this walk off of the laser beam, the angle

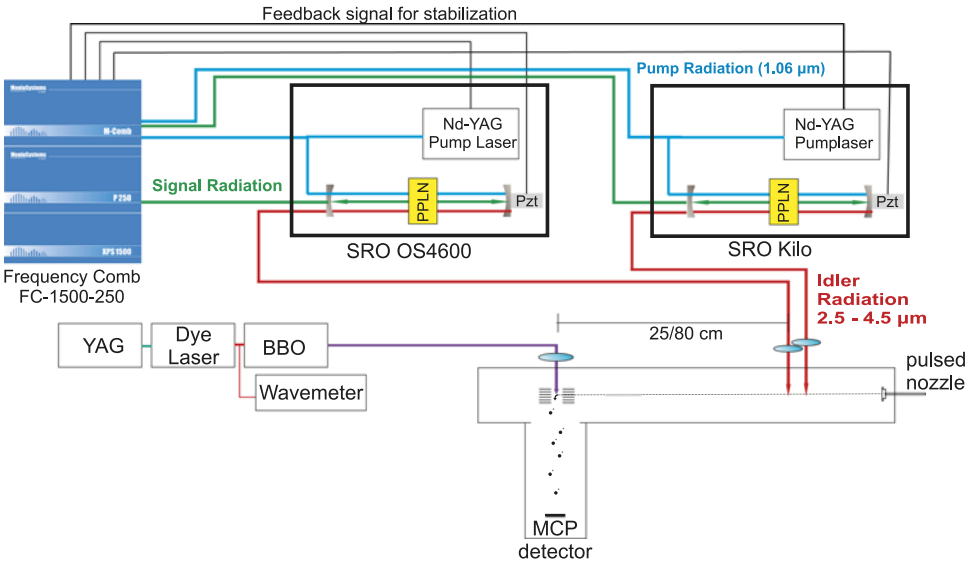

FIG. 3. Experimental setup to investigate the two step population transfer in NH_3. The two OPOs (OS4600 and Kilo, QIOPTIQ) are locked to a frequency comb (FC-1500-250, MenloSystems). The output from the two OPOs is aligned (with a spatial separation of 1–2 mm) perpendicular to the skimmed, pulsed molecular beam. After a flight path of 25 or 80 cm, the transferred population is detected by a (2+1)-REMPI process in a time-of-flight mass spectrometer (S. Kaesdorf, Munich) using a frequency doubled, YAG-pumped dye laser (NarrowScan, Radiant Dyes). Either an iodine cell or a high resolution wavemeter (Angstrom WS/6-200, High Finesse) was used for frequency calibration of the UV-radiation.

tuning of the etalon is changed to a temperature tuning of the optical path length of the laser beams through the etalon. For a 0.3 mm thick YAG etalon, a temperature range of ca. 100 K is necessary to shift the resonance of the etalon by one free spectral range (FSR) of the OPO cavity.

B. Frequency stabilization of the IR-lasers

As for the preparation step a high frequency stability is essential, the frequencies of the two lasers have to be actively stabilized. A frequency stability of 1 MHz or even better can be obtained locking the idler radiation of the OPOs to a known molecular transition or to an external cavity which in turn is locked to a frequency stabilized laser. The frequency locking to a molecular transition offers in principle a high frequency stability but only a limited number of molecular transitions are available resulting in a coarse-grained coverage of the frequency range and quite often the absolute frequency accuracy of the available spectroscopic data is limited. Through a reference cavity, in principle, every idler frequency is accessible to stabilization but the frequency stability is limited by the reference source used, e.g., a frequency stabilized HeNe-laser. Quite often several intermediate steps are necessary to obtain a well defined absolute frequency at the desired wavelength. However, a self-referenced frequency comb offers both a very high frequency stability and a very high absolute frequency accuracy, if an experimental setup with a wavemeter is available to identify the comb modes used for the frequency locking and highly stable reference to stabilize the repetition frequency. In our experiments, we use a near infrared (NIR) octave spanning frequency comb based on an erbium doped fiber laser with a repetition frequency of 250 MHz (FC1500-250, Menlo Systems).

To stabilize the frequency of the single resonant OPOs, both the pump and signal waves were phase-locked to an appropriate mode of the frequency comb. In order to lock the frequency, the radiations from the laser and from the frequency comb are superimposed collinearly on a beam splitter. Then, a narrow spectral range around the laser frequency is selected by a dispersive element like a grating or an optical bandpass filter, and the beat frequency between the laser radiation and the nearest comb mode is obtained from a fast photodiode. To increase the locking stability, the beat signal is filtered with a low-noise narrow electronic bandpass filter centered at 30 MHz. This narrow bandwidth filtering restricts the tunability of the locked laser to some MHz around the center frequency. The beat signal is split into two parts: half of the signal is sent to a frequency counter (Menlo FMX50) and the other half is used to stabilize the phase of the locked laser using a digital phase detector (Menlo DXD200). Therefore, the phase of the beat signal is compared to the phase of a signal generator (Novatech Instruments, 2918A), which is, in turn, locked to a GPS referenced rubidium clock. The register of the phase detector allows to handle phase differences of up to $\pm 64\pi$ and to generate an error signal of up to ±3.3 V, which is fed to the input of an analog PID controller (proportional-integral-derivative controller SIM960, Stanford Research).

To lock the frequency of the pump laser, two different actuators are used: The attenuated, direct output is amplified by a factor of 4 and sent to the piezo-controller of the YAG-oscillator. This allows for a control range of about ±20 MHz with a regulation bandwidth of 100 kHz. Whereas the integrated output from the PID is used to adjust the temperature of the laser crystal to account for the slow frequency drifts on a longer time scale. For the stabilization of the signal radiation, the direct output from the PID is attenuated, added to the integrated controller output, and is used to regulate the cavity length of the OPO.

If the bandpass filter behind the beat detector is removed, the beat frequency can be adjusted between 10 MHz and 75 MHz scanning the frequency of the signal generator. This allows for an independent tuning of the signal or pump wave (or of a second OPO) within a restricted range without interfering with the other frequencies.

The frequencies of the pump-, signal and idler radiation can be calculated from Equations (11)–(13):

$$\nu_{\text{pump}} = \nu_{\text{ceo}} + m_{\text{pump}}\nu_{\text{rep}} + \nu_{\text{beat,pump}}, \tag{11}$$

$$\nu_{\text{signal}} = \nu_{\text{ceo}} + m_{\text{signal}}\nu_{\text{rep}} + \nu_{\text{beat,signal}}, \tag{12}$$

$$\nu_{\text{idler}} = (m_{\text{pump}} - m_{\text{signal}})\nu_{\text{rep}} + \nu_{\text{beat,pump}} - \nu_{\text{beat,signal}}, \tag{13}$$

where ν_{ceo} is the comb offset frequency, ν_{rep} the comb repetition frequency, $\nu_{\text{beat,i}}$ the beat frequency between the pump- or signal frequency and the comb mode next to the pump- and signal frequency with the mode number m_i. The mode number for the pump and signal radiation can be obtained from a calibrated wavemeter, where the accuracy of the wavemeter has to be better than the repetition frequency of the frequency comb. From Equations (11)-(13), it can be seen that one ideal method to tune the idler frequency of one single OPO is to adjust the repetition frequency of the frequency comb and to keep the pump- and signal radiation locked to a constant beat frequency of 30 MHz. If a second OPO has to be locked or scanned independently, the scanning through the repetition rate is not any more possible and the 30 MHz bandpass filter for the pump or signal radiation of the second laser (or both lasers, if both have to be scanned) has to be removed to allow for an adjustment of the corresponding beat frequency.

The frequency stability obtained for the pump- and signal radiation of the OS4600, relative to the frequency of the frequency comb, can be derived from a histogram where the deviation of the beat signal from the reference value is measured for an integration time of 1 s. From a fit of a Gaussian distribution to the measured frequency fluctuations, a standard deviation of 1.0 Hz for the pump radiation and of 1.7 Hz for the signal radiation is obtained. For a shorter integration time of 10 ms, the frequency fluctuations increase to 72 Hz (pump) and 154 Hz (signal). However, a closer inspection of the frequency dependence of the phase noise of the pump- and signal radiation and the offset frequency ν_{ceo} of the frequency comb shows that the stability of the OPO radiation is limited by the stability of the comb offset frequency ν_{ceo}. According to Equation (13), the idler frequency is obtained as a difference of the pump and signal frequency. Therefore, it is independent on the fluctuations of the comb

offset frequency ν_{ceo}, and the absolute frequency accuracy of the idler radiation is determined by the stability of the 10 MHz rubidium Frequency Standard (FS725, Stanford Research) which is locked to a GPS reference signal (TM4, Spectrum Instruments), and the precision of the locking of the pump and signal radiation to the frequency comb. From the specified relative stability of the GPS referenced frequency standard of 10^{-12} and the locking stability, we estimate an upper limit of ±1 kHz for the uncertainty of the idler frequency, although this estimate might be considered optimistic by some.

It may be noted that in the present work on ammonia, where the detection step using the UV laser is quantum state selective, only two OPO's are used in parallel. However, in future experiments on other molecules, non-state selective UV detection may be possible[64,65] and then the third OPO can be used for preselection in the IR. In fact, a third OPO (OS4000, QIOPTIQ) was used in some experiments in the early stage of the project, although obviously not all experiments are reported in full detail here. It is a pump-enhanced single resonant optical parametric oscillator and is pumped by a 1.2 W monolithic unidirectional single mode Nd-YAG-laser (Mephisto 1200, Innolight). The maximum available power is 20 mW for the signal wave and 70 mW for the idler wave.

C. UV-laser for the REMPI detection

The REMPI detection of the prepared molecular level has been carried out by using the UV-radiation of a Nd-YAG pumped frequency doubled dye laser (injection seeded Powerlite 9010, Continuum and Narrow Scan, Radiant Dyes) with a specified spectral line width of 0.04 cm^{-1}. Using DCM (4-Dicyanomethylene-2-methyl-6-p-dimethylaminostyryl-4H-pyran) as a laser dye, a pulse energy of up to 8 mJ was obtained for the frequency doubled output between 30 000 and 34 000 cm^{-1}. Frequency calibration has been performed sending the fundamental of the dye laser to an iodine cell, and the fluorescence signal detected was calibrated against a reference standard[66] or could be measured directly by a frequency calibrated wavemeter (High Precision WS/6, High Finesse). The absolute wavenumber of the dye laser wavenumber is estimated to have an uncertainty of ±0.02 cm^{-1}.

D. Molecular beam setup and time-of-flight mass spectrometer

The molecular beam setup (Figs. 3 and 4) may be subdivided into four elements: the nozzle to generate the molecular beam, the interaction zone to prepare the molecules in the desired initial state, the flight tube for the evolution period, and the detection zone with the time-of-flight mass spectrometer. In the experiments, a pulsed nozzle with a circular aperture and 0.5 mm inner diameter is used. The pulse duration of the nozzle is set to 134 μs. The nozzle is separated by a skimmer with a diameter of 0.5 mm from the interaction zone where the population transfer due to the interaction of the molecules with the two IR-lasers takes place. The skimmer is placed 30–50 mm behind the nozzle and the distance from the skimmer to the IR-excitation was kept at 70 mm.

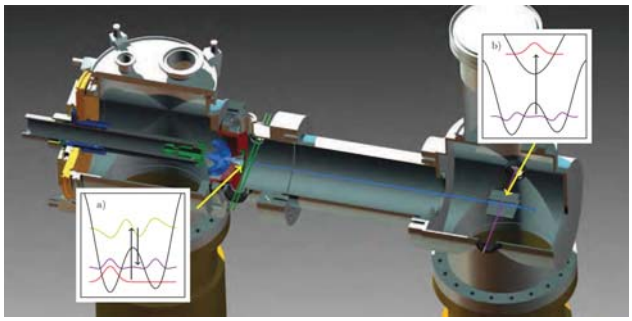

FIG. 4. Elevation design of the molecular beam setup. The molecular beam (blue) produced in a pulsed nozzle (green) is crossed by the two IR-lasers (green) to prepare the molecules in a molecular state with defined parity (inset (a)). After an evolution period defined by the passage through the flight tube, the population of the state with the opposite parity (inset (b), if applicable) is probed by resonantly enhanced multiphoton ionization with a pulsed UV-laser (violet) in a time-of-flight mass spectrometer.

For a Gaussian laser beam with a spatial intensity distribution $I(r,z)$, characterized by a beam diameter $w(z)$, the molecules are exposed during their passage through the laser beam to a temporal Gaussian laser pulse $I(z,t)$ with a pulse duration $\tau(z) = w(z)/v_{mb}$, where v_{mb} is the mean velocity of the molecules in the direction of the molecular beam. For a laser beam diameter of 0.57 mm and a molecular beam velocity of 610 m/s (see below), we obtained a pulse duration of 0.93 μs. The delay between the two IR-laser pulses in the two step (pump-dump process) experiment is obtained from $\Delta t_{pd} = \Delta x_{pd}/v_{mb}$ for a spatial separation Δx_{pd} of the two laser beams in the molecular beam direction (Δt_{pd} is typically 1-3 μs).

The free evolution time is determined by the separation Δx_{ev} of the IR-laser interaction zone from the UV-laser ionization zone in the time-of-flight mass spectrometer and the velocity of the molecular beam as $\tau_{ev} = \Delta x_{ev}/v_{mb}$. The separation of the interaction and ionization zone can be varied introducing flight tubes of different lengths. Without any additional flight tube the separation is 250 mm and was extended in the present setup to 800 mm in a first step, which results in a delay of about 1.3 ms, if Ar at room temperature is used as a seed gas.

After ionization with the UV laser, the molecular ions are detected in a two stage reflectron time-of-flight mass spectrometer (RTF10, Kaesdorf) with the flight axes perpendicular to the molecular beam. The measured ion signal for $^{15}NH_3$ and $^{14}NH_2D$ showed that there is a shift of the flight time of 2.6 ns for the two isotopomers, but for a width of the ion signal of 10 ns, the two signals cannot be resolved. The UV-laser for multiphoton ionization is focused with a f = 250 mm lens to the center of the extraction region of the time-of-flight mass spectrometer. In the focal point with a beam diameter of 0.2 mm, a laser intensity of 1.6 GW cm^{-2} is reached for the maximum pulse energy of 8 mJ, if a Gaussian intensity distribution $I(r,z)$ is assumed. As a result of the non-perfect Gaussian intensity distribution, the actual intensity may be smaller.

The molecular beam setup is pumped by 3 or 4 different turbo molecular pumps (Pfeiffer Vacuum). For a valve repetition rate of 10 Hz and a backing pressure of 2 bar,

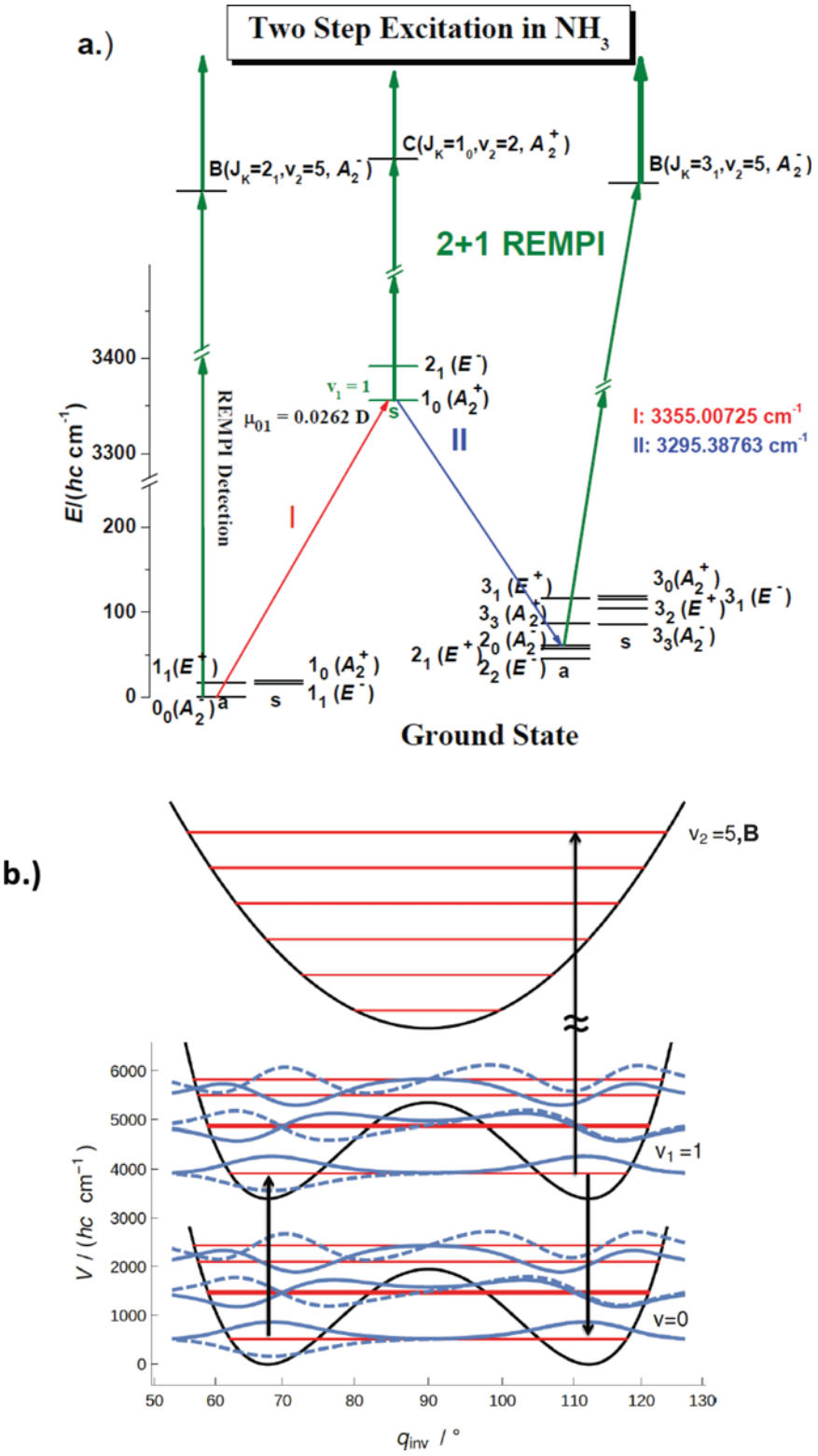

FIG. 5. (a) Scheme of some of the rovibrational levels relevant for the one and two photon population transfer in NH_3. The green line is for the REMPI detection (see Tables I–III for symmetry notation). (b) Quasi-adiabatic channel potentials of NH_3 for the lowest channel and the vibrationally excited channel with $v_1 = 1$. The vibrational energies for the 3 lowest inversion levels are shown together with the corresponding wavefunctions as supported by the effective quasiadiabatic channel potentials.

the measured pressures varied from $1.6 \cdot 10^{-8}$ mbar in the time-of-flight compartment to $1.0 \cdot 10^{-4}$ mbar in the nozzle chamber. In the interaction region and the flight tube, we obtain a pressure of $5.3 \cdot 10^{-7}$ mbar. For a collision cross section of $\sigma_{\mathrm{Ar–NH_3}} = 66$ A^2 between NH_3 and Ar, this background pressure at room temperature results in a collision free flight path of 118 m for the NH_3 molecules in the molecular beam, if collisions among the molecules of the molecular beam are neglected.

From the variation of the delay time of the ionizing UV-pulse with respect to the trigger of the nozzle for a flight path of 0.8 m, the temporal intensity profile of the molecular beam in the detection zone could be obtained. For a pulse length of 134 μs for the trigger pulse, a main peak with a width of 150 μs is obtained followed by a tail of approximately 1 ms. To derive the velocity distribution of the molecular beam, an opto-acoustical modulator (AGM-406A9M, IntraAction Corp.) was applied to generate a rectangular IR-laser pulse

with a pulse duration of 3 μs. The timing of the IR-pulse was adjusted to the maximum of the molecular beam intensity and the spread of the excited molecules arriving in the detection zone was determined by scanning the delay of the UV-laser pulse with respect to the IR-laser pulse. The velocity distribution derived from the measured time profile could be well presented by a Gaussian distribution with a mean velocity $\langle v_{\mathrm{mb}} \rangle = 610$ ms^{-1} and a width of $\Delta v_{\mathrm{FWHM}} = 70$ ms^{-1} (full width at half-maximum FWHM), which would correspond to a translational temperature of 4.2 K. When scanning the time of the IR-laser pulse with respect to the trigger pulse for the molecular beam, no significant variation of the velocity distribution was apparent.

For our experimental conditions, we estimate approximately $3.2 \cdot 10^8$ molecules in our REMPI detection volume of 2 mm^3.[67] Multiplying this number with the NH_3 mole fraction of 0.05 (see below), the transfer efficiency in the laser preparation process of 0.64 and the fraction of molecules transferred after 1.3 ms to the state with the opposite parity of $1.58 \cdot 10^{-6}$, we obtain $40/q_{\mathrm{rot}}(T_{\mathrm{rot}})$ molecules for an assumed $\Delta_{\mathrm{pv}}E/hc = 10^{-12}$ cm^{-1}, where $q_{\mathrm{rot}}(T_{\mathrm{rot}})$ is the rotational partition function at the rotational temperature T_{rot} in the molecular beam. This number could be increased substantially by reducing the molecular beam velocity, for example, with a heavier seed gas like Xe.

The repetition rate of the experiment is limited to 10 Hz by the maximum repetition rate of the Nd-YAG laser. Two delay generators (DG535, Stanford Research Systems) were used to trigger the different elements of the experiment: the nozzle of the molecular beam, the flash lamps and the Q-switch of the Nd-YAG laser, the time gate for the boxcar integrator (SR250, Stanford Research Systems) for the detectors of the fluorescence signal of the iodine cell, the UV- and the ion signal, and the data acquisition (NI-PXI6251, National Instruments).

E. Characterization of the IR-laser beams and further specifications

One crucial element of the experiment is an optimum population transfer for every step of the process, and therefore, the beam parameters of the two IR-lasers have to be well controlled. The idler beams of the two OPOs could be reasonably approximated by a Gaussian laser beam. Both idler beams are transferred by a combination of two lenses from the laser output to the point of interaction with the molecular beam in order to obtain the optimized beam parameters in the interaction region. To focus the laser beam to the molecular beam, a $f = 150$ mm lens is used. As an effective laser pulse with a temporal frequency chirp has to be applied for an optimized population transfer (see Section IV), the laser beams are adjusted with their beam waist ca. 40–50 mm before crossing the molecular beam.

An ideal Gaussian laser beam at a distance z from the beam waist is completely characterized by the complex beam parameter $q(z)$ which is defined as

$$1/q(z) = 1/R(z) - \mathrm{i}\lambda/(\pi \cdot w^2(z)), \tag{14}$$

$$\text{with} \quad w(z) = w_0 \sqrt{1 + (\frac{z\lambda}{\pi w_0^2})^2}, \tag{15}$$

$$R(z) = z(1 + (\frac{\pi w_0^2}{\lambda z})^2), \tag{16}$$

where $R(z)$ is the radius of the wavefront curvature and $w(z)$ is the beam diameter at a distance z from the beam waist, λ is the wavelength of the radiation, and $\mathrm{i} = \sqrt{-1}$. The beam profile behind the focusing lens was measured with a pyroelectric camera and a slightly elliptical beam profile has been obtained. From a fit to the experimental data, a mean beam diameter $w_0 = \sqrt{w_{0,x} w_{0,y}} = 0.57$ mm at a distance of 200 mm from the lens was derived, for example, for the OPO Kilo. At a distance of 50 mm from the beam waist, the radius of curvature R is approximately calculated from Equation (16) to 2.37 m.

For a molecular beam with a molecular beam velocity v_{mb} crossing a Gaussian laser beam with a radius of curvature R, the chirp rate $\dot{\Delta}$ of the instantaneous frequency seen by the molecules (centered at ν_0) can be calculated as[68]

$$\dot{\Delta} = \mathrm{d}\nu/\mathrm{d}t = -\frac{\nu_0 v_{\mathrm{mb}}^2}{c\,R}. \tag{17}$$

At a distance of 50 mm in front of the focal point, we obtain for the laser wavenumber of 3300 cm^{-1} and a molecular beam velocity of 610 ms^{-1} a chirp rate of $\dot{\Delta} = 2.5$ MHz/μs for an ideal Gaussian laser beam. This frequency chirp may be to some extent reduced for non-ideal Gaussian laser beams where a distortion of the wave front is expected.

The purity of ammonia with $^{14}NH_3$ in natural abundance has been validated by gas chromatography and was found to be better than 99.98%. Ar was purchased from PanGas (purity specified as 99.996%). To obtain a sufficient detection (REMPI) signal on the one hand and to reduce the probability of cluster formation on the other hand, a mole fraction of 0.05 for NH_3 was chosen for the gas mixture. The experimental results described in the present work were, in general, reproduced in at least two independent series of experiments carried out separately by independent operators of the system.

III. NH_3 AS A PROTOTYPE SYSTEM TO INVESTIGATE THE TWO STEP POPULATION TRANSFER

A. Rovibronic level structure and symmetry notation

As even the simplest chiral molecules show considerable spectroscopic complexity, we have carried out the basic experiment with a simple achiral molecule as a proof of principle for the testing of our experimental setup. The use of NH_3 as a test molecule has a number of advantages for the investigation of the efficiency of the two step population transfer required.

— NH_3 is a stable molecule with a high vapor pressure which makes it an ideal molecule for molecular beam experiments.

— The high resolution IR-spectroscopy of NH_3 is relatively well understood and allows for a proper selection of the initial, intermediate, and final level,[69] including a detailed theoretical understanding of all levels[70] (see also Ref. 71).

— In a molecular beam, only a small number of rotational levels is populated and a two step process can be used to transfer population to initially unpopulated rotational levels of well defined parity in the vibrational ground state using a vibrationally excited level as an intermediate.

— The vibrational transitions to the symmetric (ν_1) and antisymmetric (ν_3) NH-stretching vibration are intense and coincide with the spectral tuning range of our IR-lasers.

— The hyperfine structure of the rovibrational transitions resulting from the nuclear spin of the N-atom can be resolved under our experimental conditions allowing us to probe the population dynamics of hyperfine transitions.

— The REMPI spectrum of NH_3 is well understood and gives access to a straightforward interpretation of the measured population transfers.

While the equilibrium geometry of ammonia is pyramidal and corresponds to the point group C_{3v} in the electronic ground state, the large tunneling splittings lead to easily resolved tunneling doublets, which can be classified in the full permutation inversion group $S_3^* = S_3 \otimes S^*$, with the symmetric group S_3 for the permutation of the three protons and the reflection group S^*.[8] Equivalently, for this particularly simple case, one can use the D_{3h} point group notation for the planar geometry of the transition state for ammonia inversion. Tables I and II give the character tables for the molecular symmetry group M_{S6} isomorphous to C_{3v} following Longuet Higgins[72] and for S_3^* (D_{3h}).

We give in Table I the induced representation $\Gamma(M_{S6} \uparrow S_3^*)$ which defines the symmetry species of the tunneling doublets derived from a level of given symmetry in C_{3v}. We use the systematic notation of Refs. 8 and 73–75, which assigns a well defined species (A_1, A_2, E or [3], [1^3], [2,1]) in S_3 and indicates positive or negative parity (for the symmetry species in the reflection group S^*) by a superscript + or −. This defines the notation used here and we give also the notation for the corresponding species in D_{3h} in Table II, which is also quite common (see Ref. 76). We also give the common notation s and a for the "symmetric" and "antisymmetric" tunneling sublevels, where the symmetry refers to the parity of the vibrational wavefunction with respect to the inversion plane (see also Refs. 77 and 78). The corresponding combinations with the rotational quantum numbers J and K (labeled J_K) are given in Table III together with the relevant nuclear spin statistical weights g_{JK} for $^{14}NH_3$. The ^{14}N nucleus has positive parity[65,74] as have the protons, and thus, the parities of the rovibrational levels indicate total parity. Table IV gives a summary of the lowest rovibrational-tunneling sublevels of $^{14}NH_3$ with their energies, symmetries, and nuclear spin statistical weights. This table provides also the thermal populations of these levels at 5 K and 10 K calculated with the limiting assumptions of either nuclear spin symmetry conservation[73] which is the case most commonly found with relaxation in a supersonic expansion, or with complete nuclear spin symmetry relaxation, i.e., perfect thermal equilibrium among all levels. Parity sublevels are assumed to reach thermal equilibrium in both models as it is generally found that parity may change easily upon collisional relaxation.[79]

The population distribution of the rotational levels of NH_3 after the expansion in a molecular beam has been investigated repeatedly by different groups. To ascertain beyond doubt whether the nuclear spin symmetry for NH_3 is conserved or whether a complete relaxation of the nuclear spin symmetry takes place during the expansion, a rotational temperature below 20 K has to be reached. In their diode laser spectra of the ν_2-mode Hepp *et al.*[80] found some evidence for only partial nuclear spin symmetry relaxation for the expansion of an Ar/NH_3 mixture. The (2+1)-REMPI spectra of Kay and Grimley[81] showed a higher rotational temperature for the ortho nuclear spin symmetry isomer as compared to the para-nuclear spin isomer. The intensities of the

TABLE I. Character table of the subgroup M_{S6} of the molecular symmetry group M_{S12} (S_3^*) and induced representation $\Gamma_m \uparrow S_3^*$. M_{S6} is isomorphous to C_{3v} (for which we use the same symbols for the species).

C_{3v}	E	$2C_3$	$3\sigma_v$	
M_{S6}	E	2(123)	$3(12)^*$	$\Gamma(M_{S6}) \uparrow S_3^*$
A_1	1	1	1	$A_1^+ + A_2^-$
A_2	1	1	−1	$A_2^+ + A_1^-$
E	1	−1	0	$E^+ + E^-$

TABLE II. Character table of the subgroup M_{S12} (S_3^*) isomorphous to the point group D_{3h}. The first three columns provide the species following three different notations (1: [partition]^{parity} for S_3^*, 2: [S_3 species]^{parity}, 3: D_{3h} point group species, see text).

	D_{3h}		E	$2C_3$	$3C_2$	σ_h	$2S_3$	$3\sigma_v$
	S_3^*		E	2(123)	3(12)	E^*	$2(123)^*$	$3(12)^*$
	$\Gamma(S_3^*)$	$\Gamma(D_{3h})$						
$[3]^+$	A_1^+	A_1'	1	1	1	1	1	1
$[1^3]^+$	A_2^+	A_2'	1	1	−1	1	1	−1
$[2,1]^+$	E^+	E'	2	−1	0	2	−1	0
$[3]^-$	A_1^-	A_1''	1	1	1	−1	−1	−1
$[1^3]^-$	A_2^-	A_2''	1	1	−1	−1	−1	1
$[2,1]^-$	E^-	E''	2	−1	0	−2	1	0

TABLE III. Notation for symmetry species in the totally symmetric vibronic (ground state) level for rotational quantum numbers J and K and nuclear spin statistical weights g_{JK} (see also Ref. 77 for ND_3, where all levels are Pauli allowed with non-zero nuclear spin statistical weights).

Symmetry[a]	J	K	g_{JK}	$(I_{Htot})^b$
s,a; A_1^+,A_1^-	all	3,6,9,12,…[c]	0	(…)
s,a; A_2^+,A_2^-	all	3,6,9,12,…	12	(3/2)
s,a; E^+,E^-	all	1,2,4,5,…[d]	6	(1/2)
a; A_1^-	odd	0	0	(…)
a; A_2^-	even	0	12	(3/2)
s; A_1^+	even	0	0	(…)
s; A_2^+	odd	0	12	(3/2)

[a]s and a give pure vibrational parity, $A_{1,2}^{\pm}$, $E^{\pm}$ the total rovibrational species of the level..
[b]In parentheses, the total nuclear spin I_{Htot} for the 3 protons is given.
[c]K-doublets ($A_1 + A_2$) have positive rotational parity for K = 6, 12, 18, … (even 3n) and negative rotational parity for K = 3, 9, 15, … (odd 3n).
[d]The rotational parity is positive for K = 2, 4, 6, … (even) and negative for K = 1, 5, 7, … (odd).

TABLE IV. Symmetry, energy, and relative population of the lowest rotational states at $T_{rot} = 5$ K and $T_{rot} = 10$ K in NH_3. "nc" stands for nuclear spin symmetry conservation and "nr" for complete nuclear spin symmetry relaxation during the expansion.

J	K	v-symmetry	vr-symmetry	g_{JK}	(E/hc)/cm^{-1} [144]	p^{nc}_{JK}(5 K)	p^{nr}_{JK}(5 K)	p^{nc}_{JK}(10 K)	p^{nr}_{JK}(10 K)
0	0	a	A_2^-	12	0.7934	0.494	0.957	0.419	0.661
1	1	s	E^-	6	16.1723	0.278	1.72×10^{-2}	0.256	0.108
1	1	a	E^+	6	16.9627	0.222	1.37×10^{-2}	0.228	9.68×10^{-2}
1	0	s	A_2^+	12	19.8899	6.09×10^{-3}	1.18×10^{-2}	8.06×10^{-2}	0.127
2	2	s	E^+	6	44.7945	1.23×10^{-4}	7.59×10^{-6}	6.94×10^{-3}	2.94×10^{-3}
2	2	a	E^-	6	45.5858	9.78×10^{-5}	6.05×10^{-6}	6.19×10^{-3}	2.62×10^{-3}
2	1	s	E^-	6	55.9381	4.98×10^{-6}	3.08×10^{-7}	1.40×10^{-3}	5.92×10^{-3}
2	1	a	E^+	6	56.7086	3.99×10^{-6}	2.46×10^{-7}	1.25×10^{-3}	5.30×10^{-4}
2	0	a	A_2^-	12	60.4130	8.76×10^{-8}	1.70×10^{-7}	3.94×10^{-4}	6.22×10^{-4}

UV-photodissociation spectra of Bach *et al.*[82] were consistent with the assumption of nuclear spin symmetry conservation. From these published results, it is in any case justified to assume that a strong deviation from a complete nuclear spin symmetry relaxation is obtained for a noble gas/NH_3 expansion. Nuclear spin symmetry conservation is most commonly found for polyatomic molecules cooled in a supersonic jet. For H_2O, some nuclear spin symmetry relaxation was observed at high H_2O concentrations.[83] In the present work, we have not pursued this question in detail for ammonia.

The infrared spectrum in the region of the NH-stretching vibration has been analyzed by Kleiner *et al.*[84] From their measured line strengths, the fundamental vibrational transition moments $\mu(\nu_1) = 0.0262$ D and $\mu(\nu_3) = 0.0182$ D are derived in good agreement also with theory.[70] An energy level scheme with the relevant rovibrational states together with some of the probed transitions is shown in Figure 5.

The UV-spectrum of NH_3 has been extensively studied by linear UV-absorption spectroscopy[85,86] and by (2+1)- and (3+1)-REMPI.[87–89,81,90–92] The lowest three electronically excited states are summarized in Table V together with their symmetry in D_{3h} and excitation energy relative to the electronic ground state. The spectra of most of the electronically excited states show a long progression in the vibrational ν_2-mode (inversion mode), as the excited states have planar equilibrium geometries. To determine the population of the rovibrational levels before and after IR-laser excitation, we have used (2+1) resonantly enhanced multiphoton ionization. The selection rules for the rotational quantum numbers in NH_3 for the (2+1)-REMPI two photon step are identical to the ones of the Raman transition of symmetric top molecules.[93,94] For the 2-photon excitation to the $\tilde{C}(A_1')$-state, the selection rules are $\Delta J = 0, \pm 2$ and $\Delta K = 0$ and to $\tilde{B}(E'')$-state, we get $\Delta J = 0, \pm 2$ and $\Delta K = \pm 1$ or $\Delta J = 0, \pm 2$ and $\Delta K = 0, \pm 2$ depending on the symmetry of the initial and final vibrational states. However, for NH_3, the transitions with $\Delta K = \pm 2$ have never been observed in a (2+1)-REMPI spectrum. We also note the rigorous rovibronic selection rule that in the Goeppert Mayer type two photon transitions, both parity and nuclear spin symmetries are conserved.[95] The transitions from vibrational states with A_1'-symmetry in the electronic ground state are strongly allowed to the vibrational states with an even number of quanta in the ν_2-mode of the $\tilde{B}$- and $\tilde{C}$-state and from vibrational states with A_2''-symmetry with an odd number of quanta in ν_2.

TABLE V. Energy of the 3 lowest electronically excited states in NH_3 relative to the electronic ground state.[87,146]

Electronic state	Symmetry (D_{3h})	$\tilde{\nu}$/cm^{-1}
$\tilde{X}$	A_1'	0
$\tilde{A}$	A_2''	46 181
$\tilde{B}$	E''	59 225
$\tilde{C}$	A_1'	63 866

For experimental reasons, a range between 60 000 and 65 000 cm^{-1} was chosen for the two photon energy of the REMPI detection. Within this energy range, the vibrational states $\upsilon_2 = 1$–6 of the electronically excited $\tilde{B}$-state and the $\upsilon_2 = 0,1$ vibrational states of the $\tilde{C}$-state are accessible from the vibrational ground state. An example of a REMPI spectrum of NH_3 without IR-laser excitation is shown in Figure 6. If the full UV-laser pulse energy of 8 mJ is used and the UV-radiation is focused to the center of the extraction region of the time-of-flight mass spectrometer, the measured REMPI lines are significantly broadened and shifted due to power broadening and AC-Stark shift. To avoid the broadening of

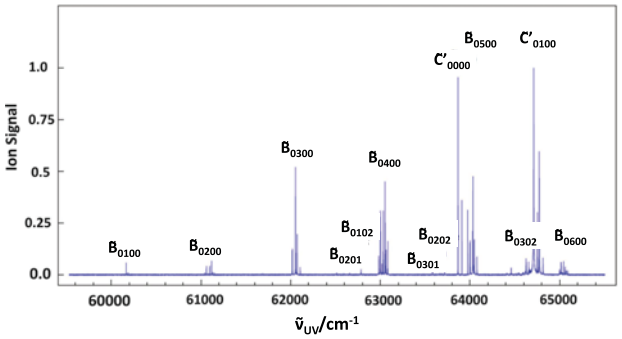

FIG. 6. (2+1)REMPI spectrum of the $\tilde{B}$- and $\tilde{C}$-states of NH_3 measured in the molecular beam without IR-laser excitation. The ion signal is normalized to the most intense line and shown as a function of the two photon wavenumber $\tilde{\nu}$. Experimental conditions: 5% NH_3 in Ar, backing pressure 2 bars, UV-pulse energy: 5 mJ. The indices to the electronic state symbol give the vibrational quantum numbers, i.e., Y_{v_1,v_2,v_3,v_4} indicates that in the Y state, the vibrational quantum numbers are (v_1, v_2, v_3, v_4), where all transitions originate from the vibrational ground state.

the ion signal, the pulse energy is reduced to between 1 and 2 mJ in most of the experiments and the focus of the UV-radiation is placed 3–4 cm behind the center of the extraction zone.

B. Hyperfine level structure and selection rules

The model calculations for the simplified three level system in Section IV show that the imperfect population transfer resulting from Rabi oscillations can be eliminated if the order of the pump and dump (Stokes) pulse is exchanged in a Stimulated Raman Adiabatic Passage (STIRAP) process or if chirped laser pulses are applied in a Rapid Adiabatic Passage (RAP) process. For a realistic theoretical description of the population transfer process in NH_3, the relatively wide hyperfine structure resulting from the nuclear spin of the nitrogen atom ($I(^{14}N) = 1$) has to be taken into account. The hyperfine splitting due to ^1H is very small, indeed, and can be neglected here. Including only the ^{14}N-part part of the hyperfine structure, the total angular momentum $\vec{F}$ is calculated from the vector sum of the rotational angular momentum $\vec{J}$ and the nuclear spin $\vec{I}$,

$$\vec{F} = \vec{J} + \vec{I}, \quad F = J + I,\ J + I - 1, \ldots, |J - I| + 1,\ |J - I|. \tag{18}$$

The wave function of a given hyperfine level in the vibrational state v may then be described by $\Phi_{vJKFI} = |vJKFI\rangle$ and the energy eigenvalues for the hyperfine levels are obtained from the simplest approximation for term values of a symmetric top, where the quadrupole nucleus is on the C_3 symmetry axis,[96,97]

$$\langle vJKFI|H_Q|vJKFI\rangle = eQq_v[\frac{3K^2}{J(J+1)} - 1]\ \frac{0.75\,C(C+1) - I(I+1)J(J+1)}{2(2J-1)(2J+3)I(2I-1)} \tag{19}$$

with

$$C = F(F+1) - J(J+1) - I(I+1), \tag{20}$$

where eQq_v is the quadrupole coupling constant of the vibrational state v in common notation.[74,97,98]

For linearly polarized laser light, as used in our work, only transitions with $\Delta m_F = 0$ are allowed and the transition moments between the components of the different hyperfine levels of a vibrational transition are given by[98]

$$\left\langle v'J'K'F'm'_F I'\right| \mu \left|vJKFm_F I\right\rangle = \delta_{I',I}(-1)^{F'+F+I-K-m_F+1}\sqrt{(2F+1)(2F'+1)(2J+1)(2J'+1)}$$
$$\times \begin{pmatrix} F' & 1 & F \\ -m_{F'} & 0 & m_F \end{pmatrix} \begin{Bmatrix} J' & F' & I \\ F & J & 1 \end{Bmatrix} \begin{pmatrix} J & 1 & J' \\ K & q & K' \end{pmatrix} \langle v'|\, \mu_{v,v'}\, |v\rangle \tag{21}$$

with $\langle v'|\, \mu_{v,v'}\, |v\rangle$ being the vibrational electric dipole transition moment and q determines the ΔK selection rules, where we obtain $q = 0$ for the $A'_1 \leftrightarrow A'_2$ and q = ±1 for the $A'_2 \leftrightarrow E'$ vibrational transition considered for D_{3h}-symmetry (for the vibrational transitions relevant in our experiments). The expressions in the large parentheses represent the Wigner-6j ({}) and Wigner-3j (()) symbols. From the coupling matrix elements, we get the selection rules $\Delta I = 0$ and $\Delta F = 0, \pm 1$ for the hyperfine transitions.

In Table VI, the reduced eigenvalue matrix for the hyperfine levels of the three rovibrational levels is given. The $J_K = 0_0$ rotational state is not split by the quadrupole interaction, but for the J ≠ 0 rotational states, three hyperfine sublevels are obtained (F = J-1, J, J+1). For the vibrational ground state, the quadrupole coupling constant ($eQq_0 = -4089.8$ kHz) is taken from Ref. 99 whereas for the vibrationally excited state, the experimental value ($eQq(v_1 = 1, J_K = 1_0, s, A_2^+) = -4024.6$ kHz) from Section VI was used. The electric dipole coupling matrix calculated according to Equation (21) using the vibrational transition moment of Sec. III A is given in Table VII. These data are used for the calculations of the population transfer in Section IV.

IV. METHODS FOR AN EFFICIENT POPULATION TRANSFER IN A THREE LEVEL SYSTEM AND MODEL CALCULATIONS

A. General aspects

In a first approximation, the preparation step for the $\Delta_{pv}E$ experiment, the absorption of a photon, and the following stimulated emission of a second photon can be described by a three level system, coupled by two different laser pulses. The pump laser excites the population from level $|1\rangle$ to level $|2\rangle$ from where it is transferred to level $|3\rangle$ by the dump (or "Stokes") laser. The simplified level scheme for the electronic ground state of NH_3 is shown in Figure 5 together with one possible two step excitation process and the corresponding REMPI probing of the transferred population. For an optimized choice of the laser parameters, the population would be transferred completely from level $|1\rangle$ to level $|3\rangle$.

To calculate the efficiency of the transfer process, the time dependent Schrödinger equation has to be integrated for a given set of molecular and laser parameters,

$$i\hbar\frac{\partial}{\partial t}\Psi(\mathbf{r},t) = \hat{H}(t)\Psi(\mathbf{r},t), \tag{22}$$

TABLE VI. Reduced term eigenvalues ν_{red} in MHz for the hyperfine levels of the three NH_3 levels included in the population transfer (rovibrational levels: $\nu_{|000\rangle} = 0.7934\ cm^{-1}$, $\tilde{\nu}_{|110\rangle} = 3055.8007\ cm^{-1}$, $\tilde{\nu}_{|020\rangle} = 60.4130\ cm^{-1}$, thus, $\nu_i = c\tilde{\nu}_{|vJK\rangle} + \nu_{red,i}$).

$\|vJKFI\rangle$	$\|00011\rangle$	$\|11001\rangle$	$\|11011\rangle$	$\|11021\rangle$	$\|02011\rangle$	$\|02021\rangle$	$\|02031\rangle$
$\|00011\rangle$	0	0	0	0	0	0	0
$\|11001\rangle$	0	2.012[a]	0	0	0	0	0
$\|11011\rangle$	0	0	−1.006[a]	0	0	0	0
$\|11021\rangle$	0	0	0	0.201[a]	0	0	0
$\|02011\rangle$	0	0	0	0	1.020[b]	0	0
$\|02021\rangle$	0	0	0	0	0	−1.020[b]	0
$\|02031\rangle$	0	0	0	0	0	0	0.292[b]

[a]Obtained from the quadrupole coupling constant eQq of Table IX.
[b]Obtained from the quadrupole coupling constant eQq of the $J_K = 2_1$ state from Refs. 115–117.

TABLE VII. Electric dipole coupling matrix elements in D between the hyperfine components of the three rovibrational levels of NH_3 included in the population transfer model.

$\|vJKFI\rangle$	$\|00011\rangle$	$\|11001\rangle$	$\|11011\rangle$	$\|11021\rangle$	$\|02011\rangle$	$\|02021\rangle$	$\|02031\rangle$
$\|00011\rangle$	0	0.0151	0.0262	0.0338	0	0	0
$\|11001\rangle$	0.0151	0	0	0	0.0214	0	0
$\|11011\rangle$	0.0262	0	0	0	0.0185	0.0321	0
$\|11021\rangle$	0.0338	0	0	0	0.0468	0.0185	0.0438
$\|02011\rangle$	0	0.0214	0.0185	0.0048	0	0	0
$\|02021\rangle$	0	0	0.0321	0.0185	0	0	0
$\|02031\rangle$	0	0	0	0.0438	0	0	0

where the Hamilton operator $\hat{H}(t)$ can be split into three parts, within the semiclassical approximation, i.e., treating the field classically, which is a good approximation under our conditions,

$$\hat{H}(t) = \hat{H}_0 + \hat{H}_P(t) + \hat{H}_S(t), \tag{23}$$

where $\hat{H}_0$ is the Hamilton operator of the isolated molecule and $\hat{H}_I(t) = \hat{H}_P(t) + \hat{H}_S(t)$ describes the interaction of the molecules with the laser fields of the pump- (P) and probe (Stokes,S) lasers. In the electric dipole approximation, the interaction between the molecules and the laser field is given by

$$\hat{H}_P(t) + \hat{H}_S(t) = \hat{H}_I(t) = -\hat{\mu}_I\, E_I(t), \tag{24}$$

$$E_I(t) = \sum_i E_{i0}(t)\, \cos(\omega_i t - \eta_i), \tag{25}$$

with the molecular electric dipole operator $\hat{\mu}_I$ for the molecule and the time dependent amplitude of the laser fields $E_{i0}(t)$, the laser angular frequency ω_i, and a phase η_i.

We expand the molecular wave function $\Psi(\mathbf{r},t)$ in the basis of the eigenfunctions $\Phi(\mathbf{r})$ of the molecular system obtained from the solution of the time independent Schrödinger equation of the isolated molecule (being restricted to N levels)

$$\hat{H}_0\Phi_k(\mathbf{r}) = E_k\Phi_k(\mathbf{r}) = \hbar\omega_k\Phi_k(\mathbf{r}), \tag{26}$$

$$\Psi(\mathbf{r},t) = \sum_{k=1}^{N} b_k(t)\,\Phi_k(\mathbf{r}), \tag{27}$$

and introducing this expansion into the Schrödinger equation (22), we get

$$i\hbar\frac{d}{dt}b_i(t) = \sum_j H_{ij}\, b_j(t), \tag{28}$$

$$H_{ij}(t) = \langle\Phi_i|\hat{H}(t)|\Phi_j\rangle. \tag{29}$$

Effective dipole coupling matrix elements are calculated with the laser intensity I(t) in Equation (30) as $V_{ij} = H_{ij}/\hbar$,[95]

$$V_{ij}/s^{-1} = 8.683 * 10^7(\mu_{ij}/\mathrm{D})\sqrt{I(t)/\mathrm{W\,cm^{-2}}}. \tag{30}$$

As the number N of levels included in our treatment is small (in the simplest model 3), the set of coupled Equation (28) has been solved by direct numerical integration, making use of the rotating wave approximation in a standard way.[95,100–102] For more complex cases, one could transform to the quasiresonant picture and integrate in the Floquet or related approaches.[100]

The time dependent level populations $p_i(t) = b_i(t)\, b_i^*(t)$ are obtained with the initial population $p_1(t = 0) = 1$, which amounts to treating only the near-resonant system of coupled levels in the case of a thermal ensemble, the other populated levels being essentially unaffected by the far off-resonant radiation of modest intensity. For the time integration with the time dependent $E_{i0}(t)$, we present the Gaussian laser pulse by a series of step functions with a constant laser intensity in the sufficiently small time intervals $[t,t + \Delta t]$. We shall treat below in particular irradiation with linearly polarized light.

If the pulse area A of the laser pulses applied, defined as $A(t) = \int_{-\infty}^{t} V_{ij}(t')dt'$, is large enough to allow for an efficient population transfer, an oscillatory behavior of the level population due to Rabi oscillations is obtained. However, a complete population transfer from level $|1\rangle$ to level $|3\rangle$

is possible if an ideal π-pulse (or a $(2n+1)\pi$-pulse)[101] for the pump- and the dump (Stokes) step is used with a sufficient delay between the two laser pulses. But because the experimental laser fluence $F(\mathbf{r})$ is not constant across the interaction volume and as the condition for such a pulse design is difficult to maintain due to fluctuations of the laser pulse energy, more stable methods have to be used to obtain a complete population transfer from the initial level $|1\rangle$ to the final level $|3\rangle$. Two methods have been widely used to obtain a complete population transfer in a three level system, even for strong fluctuations of laser conditions, as discussed in Sec. IV B. We should mention here also the recent work of Zare and coworkers on efficient population transfer in H_2 by laser excitation, see Ref. 103 and further references cited therein.

B. RAP and STIRAP for population transfer

A particularly simple method to obtain a stable and complete population transfer which is largely insensitive to changes of the laser parameters has been investigated by Reuss and coworkers.[68,104,105] For the RAP population transfer, a chirped laser pulse has to be applied separately for each transition. For the RAP transfer, the pump pulse has to precede the Stokes (dump) pulse. The condition for a perfect adiabatic transition from a level $|i\rangle$ to a level $|j\rangle$ can be written as[68]

$$\left|\frac{dV_{ij}}{dt}\Delta_{ij} - V_{ij}\frac{d\Delta_{ij}}{dt}\right| \ll 2\Omega_{ij}^3, \tag{31}$$

where $\Delta_{ij}(t) = (E_j - E_i)/\hbar - \omega_l(t)$ is the time dependent resonance defect for the transition and $d\Delta_{ij}(t)/dt$ results from the (linear) chirp applied to the laser frequency ω_l. $\Omega_{ij}(t)$ is the generalized Rabi frequency which is given by (assuming real V_{ij})

$$\Omega_{ij}(t) = \sqrt{V_{ij}^2(t) + \Delta_{ij}^2(t)}. \tag{32}$$

Another interesting method is the STIRAP, pioneered by Bergmann and coworkers[106,102] to populate efficiently an atomic or molecular level which is accessible only by a two photon transition. To derive the conditions for an efficient population transfer, the basis of the molecular eigenstates $|i\rangle$ is transferred to the basis of the dressed states of the 3-level matter-field system $|a^i\rangle$, using the notation of Refs. 106 and 102,

$$|a^+\rangle = \sin\Theta\sin\Xi\,|1\rangle + \cos\Xi\,|2\rangle + \cos\Theta\sin\Xi\,|3\rangle, \tag{33}$$

$$|a^0\rangle = \cos\Theta\,|1\rangle - \sin\Theta\,|3\rangle, \tag{34}$$

$$|a^-\rangle = \sin\Theta\cos\Xi\,|1\rangle - \sin\Xi\,|2\rangle + \cos\Theta\sin\Xi\,|3\rangle, \tag{35}$$

where Ξ is a known function of the dipole coupling matrix elements V_P and V_S and the frequency offsets Δ_P and Δ_S[107] and the time-varying mixing angle Θ is given by the ratio of the coupling matrix element $V_P(t)$ of the pump pulse and $V_S(t)$ of the Stokes pulse

$$\tan\Theta(t) = V_P(t)/V_S(t). \tag{36}$$

It follows from Equations (33)-(35) that a complete population transfer from level $|1\rangle$ to level $|3\rangle$ is obtained if the mixing angle Θ is changed from 0 to $\pi/2$ during the excitation. This is equivalent to the following conditions:

$$\lim_{t\to-\infty}\tan\Theta(t) = 0, \qquad \lim_{t\to\infty}\tan\Theta(t) = \infty \tag{37}$$

which are satisfied, if the Stokes (dump) pulse precedes the pump pulse. In addition, it has been shown that for a Gaussian pulse shape, the lowest losses for a non-adiabatic transfer to the $|a^+\rangle$ or $|a^-\rangle$ state are obtained when the delay between the Stokes (dump) pulse and the pump pulse equals the laser pulse width.[106,102]

To compare the efficiency of the three different excitation methods (no chirp, chirp, and STIRAP), model calculations were done for a two step transition in NH_3. The molecular parameters are taken for a process where the molecules are excited from the $J_K = 0_0$ state of the vibrational ground state to the $J_K = 1_0$ state of the ν_1 fundamental and then transferred by the second laser to the $J_K = 2_0$ state of the vibrational ground state (Figure 5). The vibrational transition moment for the transition to the $v_1 = 1$ state is taken as 0.0262 D.[84] Comparable to the experimental conditions of Section V, we have chosen a pulse duration of 1.3 μs and a laser intensity of 60 W cm^{-2} for the pump pulse and of 50 W cm^{-2} for the Stokes pulse, which corresponds to a pulse area of $11 \pm 1\,\pi$.

The calculated population dynamics for the three level system for the different excitation methods are shown in Figure 7. Pronounced Rabi oscillations of the level populations are obtained if the unchirped pump pulse is followed by the Stokes pulse with a time delay of 2.5 μs. If the Stokes pulse is ahead of the pump pulse by 1.5 μs, no Rabi oscillations are obtained and nearly the complete population is transferred from level $|1\rangle$ to level $|3\rangle$. Level $|2\rangle$ is only slightly populated during the time overlap of the two laser pulses. For the rapid adiabatic passage, the Rabi oscillations are already strongly damped for a linear chirp of the laser frequencies of 0.25 MHz/μs but they are strong enough to prevent a complete population transfer. The Rabi oscillations almost vanish for a frequency chirp of 2 MHz/μs and a nearly perfect population transfer from level $|1\rangle$ to level $|3\rangle$ is obtained. We shall show below that these conditions can be reached in our experiment. We have thus selected this approach here for the experiments described below.

C. Model calculations for population transfer including hyperfine structure

The population dynamics of the three level system including the hyperfine structure has been calculated for the RAP method and similar experimental parameters as for the simplified system above applying the same (linear) polarization of the two laser beams. The upper part of Figure 8 shows the calculated dependence of the population transferred to the final level 3 as a function of the detuning of the pump and probe laser relative to the corresponding line centers for a frequency chirp of $\dot{\Delta}_{Pump} = \dot{\Delta}_{Stokes} = 2.0\ \mu s^{-1}$, a laser beam diameter of $w_{Pump} = w_{Stokes} = 0.8$ mm, a pump laser power of 0.65 W, and probe laser power of 0.5 W. For the chosen chirp rate, the population transfer to the final state is larger than 95% if the detuning of the pump and of the probe laser is smaller than 2 MHz with respect to the corresponding line

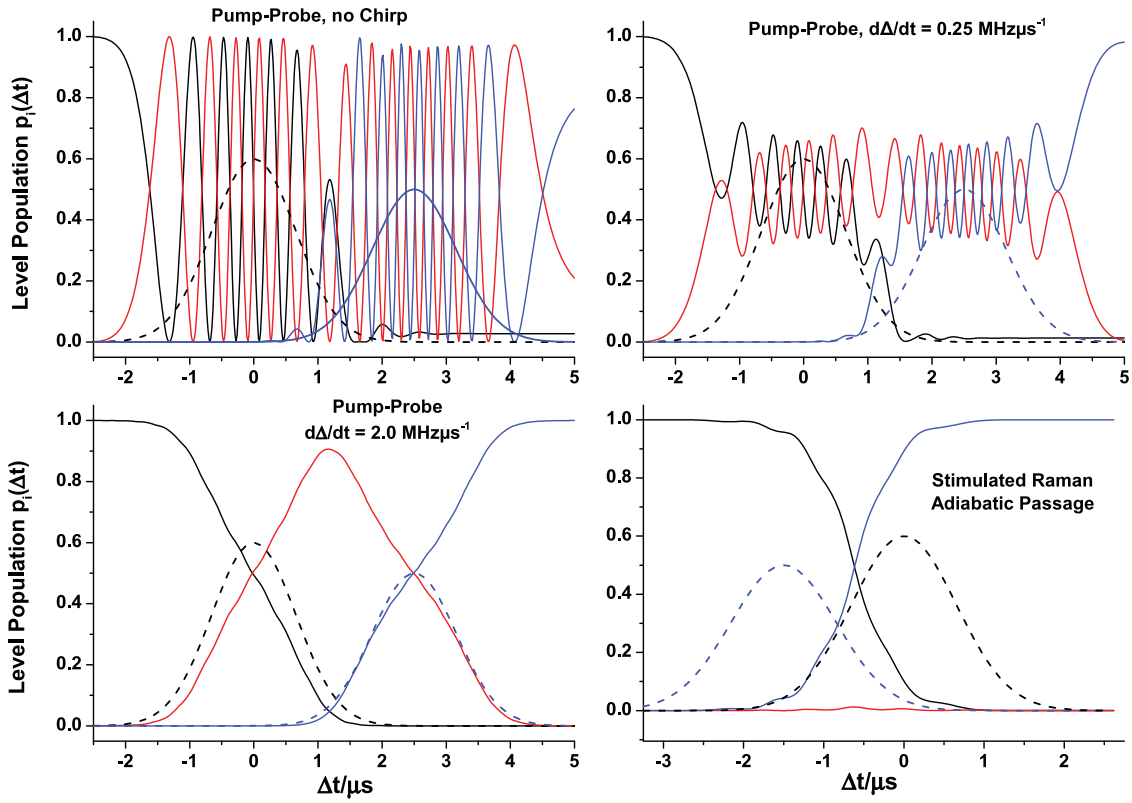

FIG. 7. Time evolution of a three level system exposed to two laser pulses nearly resonant with $|1\rangle \rightarrow |2\rangle$ and with $|2\rangle \rightarrow |3\rangle$ transition for different pulse conditions: pump-dump (Stokes), no frequency chirp (upper left), pump-dump (Stokes), small frequency chirp (0.25 MHz μs^{-1}, upper right), pump-dump (Stokes), larger frequency chirp (2.0 MHz μs^{-1}, lower left), STIRAP dump (Stokes)-pump (lower right). Time dependent level populations: $|1\rangle$: black, $|2\rangle$: red, $|3\rangle$: blue. The laser pulses are indicated by the dashed line (pump: black, dump (Stokes): blue). Experimental conditions: vibrational transition moments: $\mu_{12} = \mu_{23} = 0.0262$ D, laser power: pump: 0.6 W, Stokes: 0.5 W, pulse duration: $\tau = 1.31$ μs.

centers. The lower part of the figure shows the dependence of the population transfer to the final level on the linear chirp rates of the pump and probe laser with the center of the laser frequencies at the corresponding line position. The model calculations show that for a chirp rate larger than 0.8 MHz μs^{-1}, a stable population transfer to the final level is obtained independent of small changes of the laser beam parameter and velocity fluctuations of the molecular beam (see Equation (17)). The reduced transfer efficiency for small chirp rates as a result of the Rabi oscillations for the different coupled hyperfine levels is clearly visible. As the dipole coupling elements depend on the coupled hyperfine levels, a complex and irregular population dynamics is obtained and the Rabi oscillations are more or less washed out. For chirp rates larger than 0.8 MHz μs^{-1}, an efficient population transfer to the final level is obtained. Due to the asymmetric distribution of the hyperfine levels and dipole coupling matrix elements, the transfer efficiency is not completely symmetric as function of the chirp rates of the pump and the dump (Stokes) lasers.

The time delay between the Stokes- and the pump pulse is a crucial parameter in the STIRAP approach and is directly related to the molecular beam velocity ($\Delta t \sim 1/v_{mb}$). Even though the velocity distribution in a supersonic molecular beam is quite narrow, the velocity spread may result in a reduced population transfer efficiency. As shown above, the RAP method is over a large range insensitive to variations of the molecular beam velocity, and as the method is very robust to variations of the laser intensity and laser pulse duration, we decided to apply RAP in our experiments. In addition, the implementation of the method does not imply complicated manipulation of the laser beams as the molecules are exposed to a chirped laser pulse if the molecular beam does not cross the laser beam exactly in the focus but in its converging or diverging zone (see Section II E).

V. INVESTIGATION OF THE IR-LASER INDUCED POPULATION TRANSFER IN NH_3

A. One step population transfer

In the first experiment, the one photon process was investigated, the absorption of a photon to reach a vibrationally excited state. The molecules are excited from the ($J_K = 0_0$, a, A_2^-)-state of the vibrational ground state to the ($J_K = 1_0$, s, A_2^+)-state of the vibrationally excited $v_1 = 1$ state. Figure 9 shows the REMPI spectra recorded without (black) and with (red) IR-laser excitation. The "red" spectrum is shown for an IR-laser wavenumber $\tilde{\nu}_{pump} = 3355.007\,25$ cm^{-1} and an IR-laser power of $P_{pump} = 0.55$ W. Due to the IR-laser pre-excitation, a number of new lines are observed in the REMPI spectrum, where most of the additional lines can be identified as transitions from the vibrationally excited (electronic ground) state to the rovibrational levels of the electronically excited $\tilde{B}$- and $\tilde{C}$-state. As the population is removed from the vibrational ground state, the intensity of the lines in the REMPI spectrum originating from the ($J_K = 0_0$,

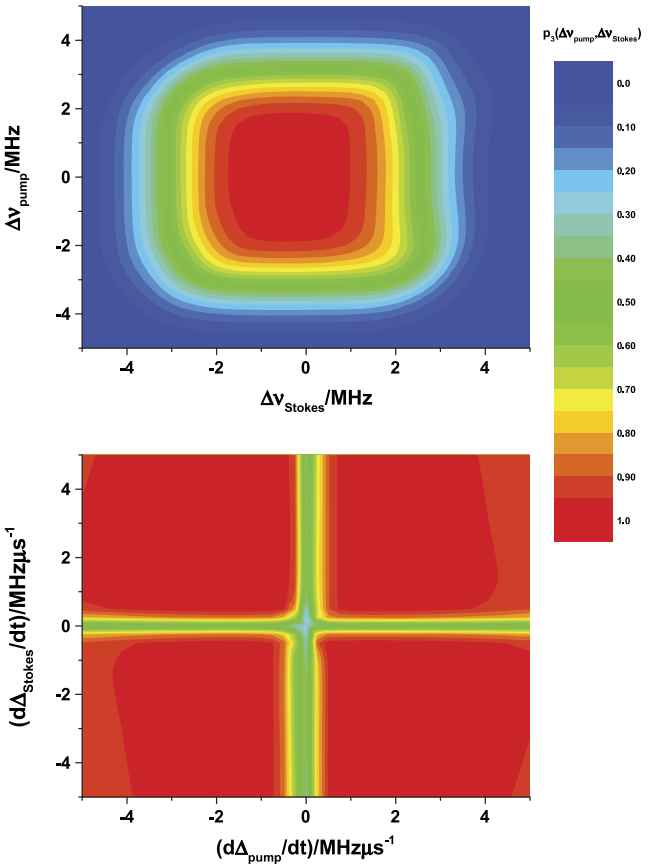

FIG. 8. Calculated efficiency of the population transfer to the final level (level 3) for the considered transfer process in NH_3 including the hyperfine structure. Laser power: pump: 0.65 W, Stokes: 0.55 W, pulse duration: $\tau = 1.31\ \mu$s. Upper part: Dependence of the transfer efficiency on the center frequency of the pump and Stokes laser with an identical chirp rate of 2 MHz μs^{-1} for both lasers. Lower part: dependence of the transfer efficiency on the chirp rate of the pump and dump (Stokes) laser with both lasers centered at the corresponding line positions.

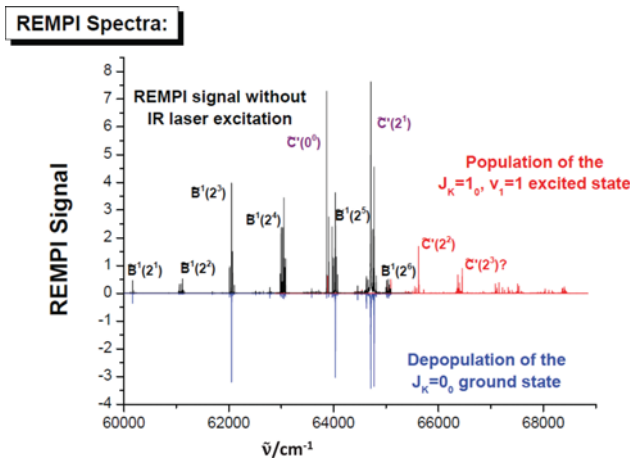

FIG. 9. (2+1)-REMPI spectrum (as relative signal strength) without (black) and with (red) one step IR-laser excitation shown as a function of the two photon wavenumber $\tilde{\nu} = E/hc$. The blue difference spectrum shows the lines originating from the ($J_K = 0_0$, a)-state of the vibrational ground state which are depopulated by the pump laser. Experimental conditions: $\tilde{\nu}_{Pump}$: 3355.007 25 cm^{-1}, IR-laser power: 0.55 W, 5% NH_3 in Ar, backing pressure 2 bar, UV-pulse energy: 1.5 mJ. The vibronic transitions use the $y(N_n^m)$ notation, where Y is the upper electronic state symbol and N_n^m gives the vibrational quantum number for the mode number N in the lower ground (the lower index 0 is omitted here) and excited (upper index m) electronic state.

a, A_2^-)-state is reduced, as can been seen from the "blue" difference spectrum in Figure 9.

To probe the depopulation of the initial state, the frequency of the REMPI-laser is set to the transition frequency from the ($J_K = 0_0$, a, A_2^-)-state of the vibrational ground state to the ($J_K = 2_1$, $v_2 = 5$, A_2^-)-state of the electronically excited $\tilde{B}$-state. The population transferred from the ($J_K = 0_0$, a, A_2^-)-state of the vibrational ground state to the ($J_K = 1_0$, $v_1 = 1$, s, A_2^+)-state is observed by tuning the REMPI laser to one of the red lines in the REMPI spectrum, for example, to the transition from the ($J_K = 1_0$, $v_1 = 1$, s, A_2^+)-state of the electronic ground state to the ($J_K = 1_0$, $v_2 = 2$, A_2^+)-state of the electronically excited $\tilde{C}$-state. Scanning the IR-laser around the transition to the ($J_K = 1_0$, $v_1 = 1$, s, A_2^+)-state, an identical line shape is obtained, independent on whether the ion signal originates from depopulation of the initial state or the population of the final state. The two spectra are shown in the upper part of Figure 10. The laser power of the IR pump laser was kept at 0.65 W. The focusing conditions of the laser beam were chosen such as to obtain a beam diameter $w = 0.8$ mm and laser chirp $\dot{\Delta} = 2$ MHz μs^{-1}. The measured population of the initial state does not completely vanish at the line center. In addition

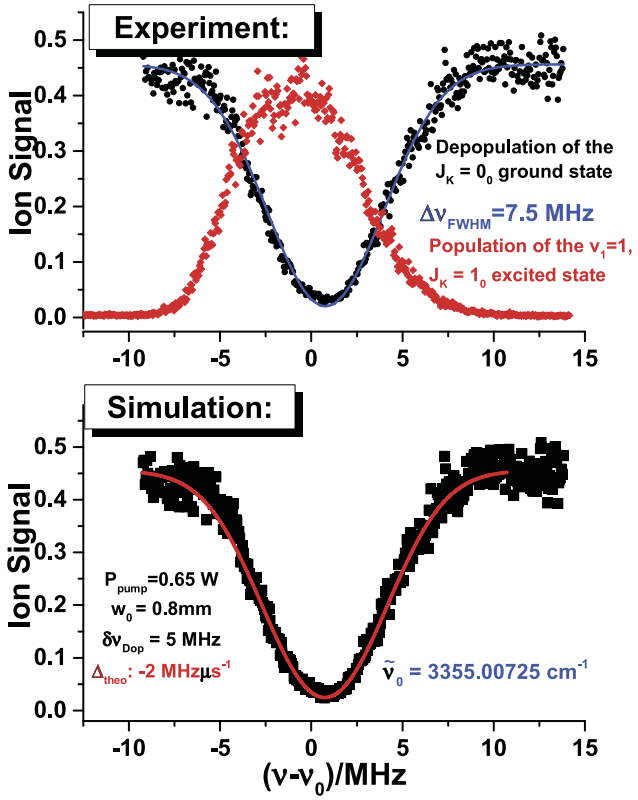

FIG. 10. Upper part: frequency dependence of the depopulation of the $J_K = 0_0$ state of the vibrational ground state measured as depletion signal on the transition to the ($J_K = 2_1$, $v_2 = 5$, A_2^-) state of the electronically excited $\tilde{B}$-state (black dots) and as population transfer to $J_K = 1_0$ of the vibrationally excited $v_1 = 1$-state measured on the transition to the ($J_K = 1_0$, $v_2 = 2$, A_2^+) state of the electronically excited $\tilde{C}$-state. The depletion signal is reduced by 90%. A fit of a Gaussian distribution to the depletion signal (blue line) results in a line width (FWHM) of 7.5 MHz. Lower part: comparison of the measured depletion signal to numerical simulations (including the hyperfine structure) for a chirp rate of 2.5 MHz (red line). To account for a residual Doppler broadening in the experiments, the simulation is convoluted with a Gaussian distribution with $\Delta\nu_{FWHM} = 5.0$ MHz.

to an incomplete population transfer, two effects might be responsible for the remaining ion signal at line center: First, population might be transferred to the initial state during the evolution period, but radiation induced population transfer due to spontaneous emission from energetically higher states and collisional population transfer from other rotational states is quite improbable. Another reason might be that the probe volume contains molecules which did not pass through the center of the IR-excitation zone, where a complete population transfer is assumed, especially as the focus of the UV-beam has been moved out of the center of the time-of-flight ionization zone and as the beam profile of the dye laser shows strong deviations from a Gaussian distribution.

The measured line widths ($\Delta\nu_{\mathrm{FWHM}}$) for both the depletion and the excitation spectrum are around 7-8 MHz. Different effects are contributing to the measured line width: the translational motion of the molecules in the direction of the laser beam, the transit time of the molecules through the laser beam, the power broadening from the laser coupling, the line broadening from the laser chirp, and finally the hyperfine structure resulting from the nuclear spin of the N-atom. An estimation shows that the contributions to the line widths for each of these effects are expected to be individually between 0.3 and 5 MHz making the measured line width of 7-8 MHz quite realistic. There is a slight frequency shift of 1-2 MHz between the measured depletion signal (black) and the measured population transfer to the vibrationally excited state (blue) resulting from a non-perfect alignment of the laser beams perpendicular to molecular beam direction. A deviation of 1° from a perpendicular direction corresponds to a frequency shift of the measured transition of 3.5 MHz for our experimental conditions.

Neglecting in a first approximation the contribution from the velocity component of the molecules in the direction of the IR-laser beam, the frequency dependence of the transferred level population is calculated from the integration of the Schrödinger equation as described in Section IV, including hyperfine structure. Using the molecular parameters for NH_3 from Tables VI and VII, the efficiency of the population transfer is calculated for a laser chirp rate of $\dot{\Delta} = 2.5$ MHz μs^{-1}, for a laser power $P = 0.65$ W, and a laser beam diameter $w = 0.8$ mm. For the experimentally determined molecular beam velocity $v_{\mathrm{mb}} = 610$ m s^{-1}, the molecules are thus exposed to a Gaussian laser pulse with $\tau_{\mathrm{pulse}} = 1.3$ μs and a laser intensity $I_0 = 65$ W cm^{-2}. To account for the residual Doppler broadening resulting from the translational motion of the molecules perpendicular to the molecular beam, the calculated depopulation curve is convoluted with a Gaussian distribution with $\Delta\nu_{\mathrm{FWHM}} = 5$ MHz, which would correspond to a perpendicular translational temperature $T_{\perp,\mathrm{trans}} = 0.08$ K for the molecules probed by the REMPI process. The calculated frequency dependence of the depopulation signal is compared in the lower part of Figure 10 to the experimental data. The comparison shows that the experimental data are well reproduced if a frequency chirp rate around 2.5 MHz μs^{-1} and a residual Doppler width of 5 MHz are assumed in the simulations of the experiments without further adjustment.

The efficiency of the one step population transfer was also investigated for the weaker overtone transition of the ν_4 mode with an increased pump laser power of 1.15 W and the same pump-probe geometry as for the excitation of the ν_1 mode. For both, the excitation of the $2\nu_4^{l=0}$ and $2\nu_4^{l\pm2}$ state efficiency was studied for the transition originating from the ($J_K = 0_0$, a, A_2^-)-state in the vibrational ground state. A transfer efficiency of 50% was obtained for the transition to the ($J_K = 1_0$, s, $v_4 = 2$, $l = 0$, A_2^+)-state and of 65% for the transition to the ($J_K = 1_1$, a, $v_4 = 2$, $l = \pm2$, E^+)-state, which both have a one order of magnitude smaller line strength as compared to the transition of the ν_1 mode. To increase the population transfer on these lines and to obtain a high efficiency on even weaker lines, the pump geometry has to be optimized, using finally a multi-path setup for further improvement.

B. Two step population transfer

To investigate the finally required two step process, the absorption of a photon followed by the stimulated emission of a second photon, the population is, again as for the one step process, transferred from the ($J_K = 0_0$, a, A_2^-)-state of the vibrational ground state to the ($J_K = 1_0$, s, A_2^+)-state of the vibrationally excited $v_1 = 1$ state, and then from there the population is transferred by stimulated emission to the ($J_K = 2_0$, a, A_2^-)-state of the vibrational ground state. Figure 11 shows the measured REMPI spectra around 64 000 cm^{-1} without (black) and with (red) population transfer due to the interaction with the two IR-lasers. For this experiment, the OS4600 with a laser power of $P_{\mathrm{pump}} = 480$ mW is tuned to $\tilde{\nu}_{\mathrm{Pump}} = 3355.007\,25$ cm^{-1} to excite the $v_1 = 1$ state and the OPO Kilo with a laser power of $P_{\mathrm{Stokes}} = 0.55$ W is tuned to $\tilde{\nu}_{\mathrm{Stokes}} = 3295.3876$ cm^{-1} to transfer the population back to the vibrational ground state.

To measure the spectral dependence of the depopulation process, the REMPI laser is tuned to the transition from the ($J_K = 1_0$, $v_1 = 1$, s, A_2^+)-state of the electronic ground

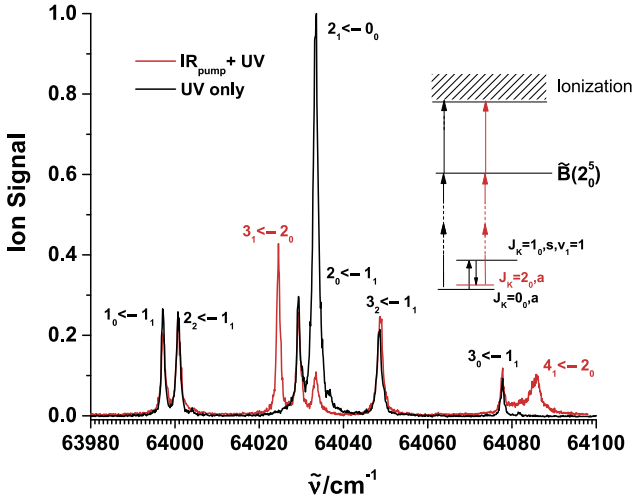

FIG. 11. Measured relative ion signal normalized to the maximum value without any IR-laser excitation (black) and after the two photon population transfer (red) shown as a function of the two photon wavenumber $\tilde{\nu}$ through the $\tilde{B}$ ($v_2 = 5$) electronically excited state. Experimental conditions: $\tilde{\nu}_{\mathrm{Pump}}$: 3355.007 25 cm^{-1}, P_{Pump}: 480 mW, $\tilde{\nu}_{\mathrm{Stokes}}$: 3295.387 63 cm^{-1}, P_{Stokes}: 550 mW, 5% NH_3 in Ar, backing pressure 2 bars, UV-pulse energy: 1.5 mJ. The rotational transitions are indicated as ($J'_{K'} \leftarrow J''_{K''}$).

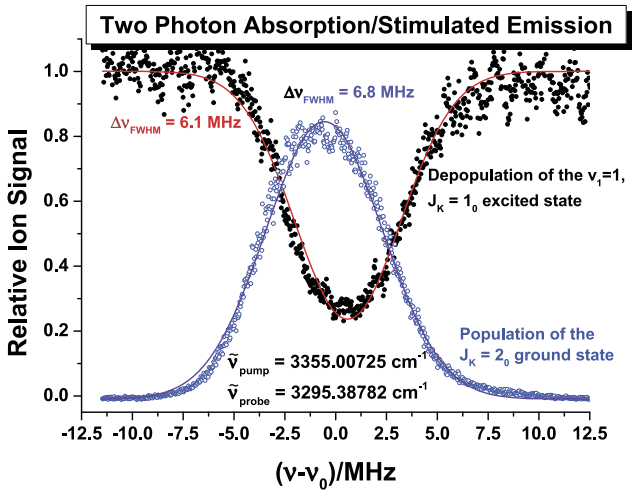

FIG. 12. Measured line shape for the depopulation signal of the vibrational excited ν_1-state ($J_K = 1_0$, s, A_2^+) as a function of the pump frequency. The black dots show the depletion of the REMPI signal, measured on the transition to the ($J_K = 1_0, v_2 = 2$, A_2^+) state of the electronically excited $\tilde{C}$-state at 62 265.42 cm^{-1}, as a function of the probe laser frequency. In the line center, the ion signal is reduced by 80%. The blue dots represent the ion signal from the ($J_K = 2_0$, a, A_2^-) state of the vibrational ground state measured on the transition to the ($J_K = 3_1, v_2 = 5, A_2^-$) state of the electronically excited $\tilde{B}$-state at 64 024.55 cm^{-1}. The red and pink lines show a fit of a Gaussian distribution function to the experimental data point resulting in line width (FWHM) of 6.1 MHz for the depletion signal and of 6.8 MHz for the population transfer to the ($J_K = 1_0$) state. Experimental conditions: $\tilde{\nu}_{Pump}$: 3355.007 25 cm^{-1}, P_{Pump}: 0.65 W; $\tilde{\nu}_{Stokes}$: 3395.387 82 cm^{-1}, P_{Stokes}: 0.55 W, $\tau_{Pulse} = 1.3$ μs, 5% NH_3 in Ar, backing pressure 1 bar, UV-pulse energy: 3.1 mJ.

state to the ($J_K = 1_0$, $v_2 = 2$, A_2^+)-state of the electronically excited $\tilde{C}$-state and the dump ("Stokes") laser for the stimulated emission is tuned across the transition with a line center at 3295.3876 cm^{-1} and the pump laser (OPO OS4600) is stabilized to the line center for the pump step at 3355.007 25 cm^{-1} with a laser power of 0.65 W. For a dump ("Stokes") laser power of $P_{Stokes} = 0.5$ W, the ion signal decreases from unity, if the dump laser is out of resonance, to 0.2 at the line center as can be seen from the black dots in Figure 12. One reason for the not perfect population transfer by the Stokes laser might be a small vertical shift of the Stokes laser relative to the pump laser.

To measure the population transferred from the vibrationally excited state ($J_K = 1_0$, $v_1 = 1$, s, A_2^+) to the ($J_K = 2_0$, a, A_2^-)-state of the vibrational ground state, the REMPI laser is tuned to the transition to the ($J_K = 3_1$, $v_2 = 5$, A_2^-)-state of the electronically excited $\tilde{B}$-state. The measured REMPI spectrum is shown with open circles in Figure 12. For both lasers, the beam diameter of w = 0.8 mm results in a pulse duration of 1.3 μs and a laser intensity of 65 W cm^{-2} for the pump laser and of 50 W cm^{-2} for the Stokes laser. The focusing conditions for both lasers were chosen such as to obtain a chirp rate $\dot{\Delta}_1 \simeq \dot{\Delta}_2 = 1.5$–2.5 MHz μs^{-1}. A Gaussian function is fitted to both experimental spectra resulting in a line width of $\Delta\nu_{FWHM} = 6$–7 MHz, nearly identical to the width for the one step process. The effective population transfer of about 64% to the final state would be largely sufficient for the scheme to measure parity violation in a suitable chiral molecule.

VI. HYPERFINE STRUCTURE IN EXCITED VIBRATIONAL LEVELS

A. General aspects

With the experimental conditions for the one step excitation process of Sec. V, it was not possible to resolve the hyperfine structure resulting from the nuclear spin of the ^{14}N-atom in the measured rovibrational transitions. In these experiments, the spectral resolution was limited by the transit time broadening, the power broadening, and the velocity component of the molecules in the direction of the laser beam, where the latter is the most significant. Increasing the laser beam diameter at the interaction region from 0.8 mm to 3.1 mm, a transit time broadening of 74 kHz is obtained for a molecular beam velocity of $v_{mb} = 610$ ms^{-1}.[108] In addition, to obtain a narrow line width, the laser chirp has to be removed completely and the laser intensity has to be reduced to avoid Rabi oscillations. To reduce the velocity component of the probed molecules in the direction of the laser beam, the flight path between the region of excitation and ionization was increased by the introduction of an additional flight tube with a length of 0.55 m resulting in a total path of 0.8 m and an additional skimmer with a diameter of 0.9 mm was placed in front of the ionization zone. With this modified experimental setup, a spectral line width of 350 kHz or better was obtained. This resolution is sufficient to resolve the hyperfine structure of the spectral lines which results from the nuclear spin of the ^{14}N-atom.

Microwave spectra of NH_3 with a resolved hyperfine structure have been obtained already in 1946 and a value for the quadrupole coupling eQq could be obtained.[109,110] This preliminary value was improved by Gunther-Mohr *et al.*, including a rough estimate of its rotational dependence and the constants D_N and D_K for the coupling of the nuclear spin of the N-atom to the molecular rotation.[111,112] With an improved experimental setup, Gordon was able to determine constants for the coupling of the hydrogen spins to the molecular rotation[113] and the mutual hydrogen spin-spin interactions could be resolved in the spectra of Kukolich *et al.*[114–116] The microwave spectra obtained by Kukolich and Wofsy have been reassigned and reinterpreted by Hougen.[117] Very precise data for the hyperfine structure in the $J_K = 1_0 \leftarrow 0_0$ transition of the vibrational ground state were obtained by Marshall and Muenter[118] and have been confirmed recently by Cazzoli *et al.*[99] with $eQq(J_K = 1_0, s) = -4089.83(2)$ kHz, the other hyperfine coupling constants being smaller by 2-3 orders of magnitude. For vibrationally excited states, the hyperfine structure has been investigated for the inversion mode ν_2 in microwave spectra[119,120] and by infrared saturation spectroscopy.[121–125] The values obtained for the quadrupole coupling constant cover a relatively wide range from eQq (ν_2,a) = −4128 kHz[120] to $eQq(\nu_2, s) = -4503.9$ kHz.[120] Generally the s-tunneling component shows a significantly higher absolute value of the quadrupole coupling constant than the corresponding a-tunneling component, when the inversion mode is excited. As a consequence of the lower resolution in the infrared (as compared to microwave range), only the constants for the coupling of nuclear spin of the N-atom to the molecular rotation could be determined, whereas the

contributions from the spin-spin couplings and the coupling of the hydrogen spin to the rotational motion could not be resolved. The hyperfine structure for the first overtone of the inversion mode $2\nu_2$ and the deformation mode ν_4 has been studied with Stark-tuned saturation spectroscopy.[126,127]

There has been also substantial theoretical work on the dependence of the hyperfine coupling constants on the vibrational state.[128–136] The dependence of the hyperfine quadrupole coupling constant upon excitation of the inversion mode in NH_3 has been specifically treated theoretically by Grigolini and Moccia and by Špirko.[128,129,133] The values calculated by Špirko are close to the higher experimental absolute values for the ν_2-mode. In agreement with the experiments, the quadrupole coupling constant is predicted to be larger for the s-tunneling component, however, with significant larger difference between the two tunneling components as compared to most of the experiments. Ha has discussed, how an accurate quadrupole moment of the ^{14}N nucleus can be derived using high level *ab initio* calculations in conjunction with spectroscopic data,[137] which thus can be useful for obtaining fundamental properties of the nuclear structure. Vibrational corrections are non-negligible in such an approach. Given the rather limited knowledge of the vibrational level dependence of the hyperfine coupling in $^{14}NH_3$, we have decided to obtain the relevant data in several vibrational states around 3300 cm^{-1} using our setup.

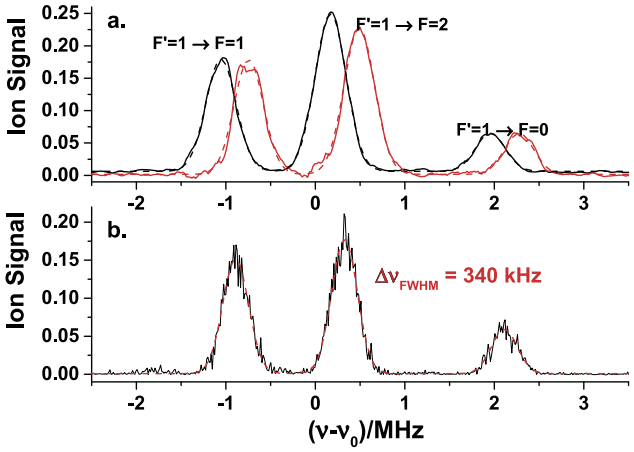

FIG. 13. High resolution spectra (as relative signal proportional to absorption) with resolved hyperfine structure for the ($J_K = 1_0$, $v_1 = 1$, s, A_2^+) ← ($J_K = 0_0$, G.S., a, A_2^-) transition. The full lines give the measured spectra for the double path experiments (black: forward direction, red: backward direction, (a)) and an ideal perpendicular single path experiment (full line, (b)). A Gaussian line shape function is fitted to the experimental spectra (dashed line) resulting in Doppler width ($\Delta\nu_{FWHM}$) of (340 ± 10) kHz for the single path experiment.

B. Hyperfine structure of the ($v_1 = 1, J_K = 1_0$, s)-state and ($v_1 = 1, J_K = 2_1$, s)-state of NH_3

Several very high resolution absorption spectra were measured with the improved setup. The absorption spectrum

TABLE VIII. Measured frequencies for the hyperfine transitions originating from the $J_K = 0_0$, a-state and $J_K = 1_1$, a-states in the vibrational ground state for different vibrationally excited states. The line position of a superposition of Doppler broadened spectra at T = 300 K is given in addition. The line positions are given with an estimated uncertainty of ±100 kHz.

Vibr. level	$J'_{K'} \leftarrow J''_{K''}$	Hyperfine transition	$\tilde{\nu}/cm^{-1}$	ν/THz
ν_1	1_0,s ← 0_0,a	F′ = 1 ← F″ = 1	3355.007 220	100.580 586 11
ν_1	1_0,s ← 0_0,a	F′ = 2 ← F″ = 1	3355.007 261	100.580 587 34
ν_1	1_0,s ← 0_0,a	F′ = 0 ← F″ = 1	3355.007 321	100.580 589 13
ν_1	1_0,s ← 0_0,a	Doppler broadened superposition	3355.007 254	100.580 587 13
ν_1	2_1,s ← 1_1,a	F′ = 2 ← F″ = 1	3374.551 291	101.166 502 64
ν_1	2_1,s ← 1_1,a	F′ = 2 ← F″ = 2	3374.551 311	101.166 503 22
ν_1	2_1,s ← 1_1,a	F′ = 2 ← F″ = 1	3374.551 330	101.166 503 80
ν_1	2_1,s ← 1_1,a	F′ = 3 ← F″ = 2	3374.551 333	101.166 503 89
ν_1	2_1,s ← 1_1,a	F′ = 3 ← F″ = 2	3374.551 377	101.166 505 19
ν_1	2_1,s ← 1_1,a	Doppler broadened superposition	3374.551 322	101.166 503 53
$\nu_3^{\pm1}$	1_1,a ← 0_0,a	F′ = 0 ← F″ = 1	3458.614 402	103.686 651 3
$\nu_3^{\pm1}$	1_1,a ← 0_0,a	F′ = 2 ← F″ = 1	3458.614 438	103.686 652 4
$\nu_3^{\pm1}$	1_1,a ← 0_0,a	F′ = 1 ← F″ = 1	3458.614 455	103.686 652 9
$\nu_3^{\pm1}$	1_1,a ← 0_0,a	Doppler broadened superposition	3458.614 438	103.686 652 4
$2\nu_4^0$	1_0,s ← 0_0,a	F′ = 1 ← F″ = 1	3235.914 443	97.010 274 5
$2\nu_4^0$	1_0,s ← 0_0,a	F′ = 2 ← F″ = 1	3235.914 545	97.010 275 5
$2\nu_4^0$	1_0,s ← 0_0,a	F′ = 0 ← F″ = 1	3235.914 478	97.010 277 5
$2\nu_4^0$	1_0,s ← 0_0,a	Doppler broadened superposition	3235.914 478	97.010 275 5
$2\nu_4^{\pm2}$	1_1,a ← 0_0,a	F′ = 0 ← F″ = 1	3251.779 670	97.485 902 0
$2\nu_4^{\pm2}$	1_1,a ← 0_0,a	F′ = 2 ← F″ = 1	3251.779 701	97.485 902 9
$2\nu_4^{\pm2}$	1_1,a ← 0_0,a	F′ = 1 ← F″ = 1	3251.779 721	97.485 903 5
$2\nu_4^{\pm2}$	1_1,a ← 0_0,a	Doppler broadened superposition	3251.779 704	97.485 903 0

TABLE IX. Summary for experimentally known and some theoretical quadrupole coupling constants eQq for different vibrationally excited states of NH_3 from the present and previous work. The values in parentheses give the uncertainties in units of the last quoted digits.

Vibrational level	Rotational transition $J'_{K''}s' \leftarrow J''_{K''}s''$	$eQq(v_i)$,s /kHz	$C_N(v_i)$,s /kHz	$eQq(v_i)$,a /kHz	$C_N(v_i)$,a /kHz	Reference technique
G.S.	1_0,s ← 0_0,a	−4089.83(2)	6.774(9)			118, MW
G.S.	1_0,s ← 0_0,a	−4089.84(70)	6.91(17)			99, MW
G.S.		−4092.40		−4087.82		129, theory
G.S.		−4091.2		−4086.4		133, theory
ν_1	1_0,s ← 0_0,a	−4024.6(26)				[This work], IR
ν_1	2_1,s ← 1_1,a	−4037(26)				[This work], IR
$\nu_3^{\pm1}$	1_1,a ← 0_0,a			−4123(29)		[This work], IR
$2\nu_4^0$	1_0,s ← 0_0,a	−4087.6(35)				[This work], IR
$2\nu_4^{\pm2}$	1_1,a ← 0_0,a			−4134(22)		[This work], IR
ν_2	2_1,s ← 1_1,a	−4429(12)		−4263(18)		119, MW
ν_2	1_0,s ← 0_0,a					
ν_2	4_3,a ← 3_3,s					
ν_2	4_2,a ← 3_2,s	−4442(156)		−4329(375)		122, IR
ν_2	4_0,a ← 3_0,s					
ν_2	8_7,s ← 7_7,a					
ν_2	3_0,s ← 3_3,a	−4495.4(31)	5.84(54)	−4440(22)	7.17(64)	123, IR
ν_2	3_3,a ← 3_3,s		$eqQ\eta_J = 27.03(58)$		−24.2(35)	double res.
			$eqQ\eta_K = -22.83(98)$		−29.5(12)	
ν_2	0_0,a ← 1_0,s					
ν_2	3_1,s ← 2_1,a					
ν_2	2_1,s ← 1_1,a	−4503.9(33)	5.41(40)	−4128(67)	6.65(61)	120, MW
ν_2	3_2,s ← 2_2,a		$eqQ\eta_J = 31.7(11)$		−26.5(89)	
ν_2	3_0,s ← 2_0,a		$eqQ\eta_K = -266(16)$		−23.9(92)	
ν_2	1_0,s ← 0_0,a					
ν_2	0_0,a ← 1_0,s	−4434.2(7)	6.43(11)			124, IR
ν_2	6_3,a ← 6_3,s			−4215(1)	ΔR = −0.535(6)	125, IR
ν_2	8_7,s ← 8_7,a	ΔeqQ = −350				121, IR
ν_2		−4454.0		−4291.5		133, theory
ν_4	2_0,a ← 2_1,a	−4040(40)				127, IR
ν_4	7_7,s ← 6_6,s			−4106(40)		127, IR
$2\nu_2$	10_9,s ← 9_9,a	−4767(80)				127, IR
$2\nu_2$	12_{10},s ← 11_{10},a	−4730(200)				127, IR
$2\nu_2$		−4827.9		−4318.6		133, theory

from the ($J_K = 0_0$, a, A_2^-)-state of the vibrational ground state to the ($J_K = 1_0$, s, A_2^+)-state of the vibrationally excited $v_1 = 1$ state was probed on the REMPI two photon transition to the ($J_K = 1_0$, $v_2 = 2$, A_2^+)-state of the electronically excited $\tilde{C}$-state and the absorption from the ($J_K = 1_1$, a, E^+)-state of the vibrational ground state to the ($J_K = 2_1$, s, E^-)-state of the vibrationally excited $v_1 = 1$ state was probed on the REMPI transition to the ($J_K = 2_1$, $v_2 = 2$, E^-)-state of the electronically excited $\tilde{C}$-state.

The accuracy of the measured position of the hyperfine transitions is limited by the residual Doppler shift resulting from the projection of the molecular beam velocity onto the propagation of the laser beam. A deviation of 1° from an exact perpendicular intersection results in a Doppler shift of 3.5 MHz. To remove this Doppler shift, two excitation spectra were measured: one spectrum was recorded with a single path of the laser beam and an additional spectrum was measured where the laser beam was exactly collinearly retro-reflected. From the difference between the spectrum with both beams and the one from the single path, the excitation spectrum of the reflected path was obtained and the true line position was calculated from the average of the absorption spectra of the two beam directions. A Gaussian line shape function was fitted to the measured lines to obtain the line positions of the different hyperfine transitions for the two paths. The measured spectra for the double path experiments are shown in Figure 13(a)

and for the single path in Figure 13(b) as calculated from the procedure mentioned above for a perfect perpendicular passage of the laser beam together with the fit of three different Gaussian line shape functions to the experimental data. The spectra shown in Figure 13 are obtained from an average of 10–15 single scans. From the remaining uncertainty of the alignment and the uncertainty of the fit of the Gaussian functions, we estimate an upper limit of ±100 kHz for the accuracy of the measured line positions, which is much larger than the uncertainty of the idler frequency of ±1 kHz of our laser (see Section II B). The measured line positions for the different hyperfine transitions of the R_0 and R_1 rotational transition of the $v_1 = 1$ vibrational mode are summarized in Table VIII (i.e., $J_K = 1_0$, s ← $J_K = 0_0$, a and $J_K = 2_1$, s ← $J_K = 1_1$, a). Also included in the table is the accurate line position for a Doppler broadened ($T = 300$ K) line obtained from a Gaussian line shape function fitted to the superposition of the three Doppler broadened hyperfine transitions. This line position would be obtained in high resolution experiments in a static cell at low pressure, however, without hyperfine resolution.

To derive the quadrupole coupling constant eQq for the measured hyperfine transitions, a model function for the line position according to Equations (19) and (20) has been used. A Gaussian line shape with an identical Doppler width for all hyperfine transitions of the measured rovibrational transition has been applied. For the ($J_K = 1_0$, s) ← ($J_K = 0_0$, a) transition, the initial state is not split and the quadrupole coupling constant of the upper state is obtained directly from the fit, resulting in $eQq(J_K = 1_0, s, v_1 = 1) = -4024.6(26)$ kHz (where the number in parentheses gives the statistical (1σ) uncertainty of the fit in units of the last digits). To derive the quadrupole coupling constant eQq for the ($J_K = 2_1$, s, $v_1 = 1$)-state, the coupling constant of the ($J_K = 1_1$,a, $v = 0$)-state determined by Hougen from the data of Kukolich has been used.[115,117] From the fit, a coupling constant $eQq(J_K = 2_1, s, v_1 = 1) = -4037(26)$ kHz is obtained. The spin-spin coupling from the H-atoms is expected to be on the order of 10 kHz[115,99,117] and is too small to be measurable in our experiments, other couplings being even smaller. The quadrupole constants derived are summarized in Table IX together with published data for the vibrational ground state and several vibrationally excited states as available from previous work.

As the accurate line positions of the hyperfine transitions are determined by a fit of three individual line shape functions to the averaged data and as the quadrupole coupling constants are obtained from a global fit based on Equations (19) and (20), the positions of the hyperfine transitions calculated with the coupling constant eQq in Table IX and the line positions given in Table VIII may differ slightly.

C. Hyperfine structure in further vibrational levels and discussion

To determine the quadrupole coupling constant for further vibrational transitions in the region of the NH-stretching vibration, the REMPI laser was set to the transition from the ($J_K = 0_0$, a, A_2^-) state of the vibrational ground state to the ($J_K = 2_1$, $v_2 = 5$, A_2^-)-state of the electronically excited $\tilde{B}$-state to detect the depletion of the initial state and to different rotational transitions to the $v_2 = 2$ vibrational state of the electronically excited $\tilde{C}$-state to probe the population transferred by the IR-pump laser to rovibrationally excited levels of the electronic ground state. Probing the population transferred to the vibrationally excited state results in background free REMPI signal with an improved signal-to-noise ratio. To improve the precision of the measured transition frequencies, the experiments were performed with the double path setup as described above. Table VIII summarizes the measured hyperfine transition frequencies. The accurate line positions have been derived from the fit of three independent Gaussian functions to the experimental data obtained from an average of 12–20 single scans. The line positions obtained from the fit of a Gaussian line shape function to the superimposed spectra of the fine structure at $T = 300$ K are also included in Table VIII.

The quadrupole coupling constants eQq for a total of 4 newly measured vibrationally excited states are included in Table IX. As all the measured transitions are originating from the ($J_K = 0_0$, a, A_2^-)-state of the vibrational ground state, the quadrupole coupling constant is directly obtained from a fit of the line positions calculated from Equations (19) and (20) as discussed above. We also give in Table IX a summary of the presently known quadrupole coupling constants in different vibrationally excited states. Figure 14 shows the measured averaged spectrum for the ($J_K = 0_0$, a, v = 0, A_2^-) → ($J_K = 1_0$, s, $v_4 = 2$, l = 0, A_2^+) transition together with a fit of Equations (19) and (20) to the experimental data.

From the summary in Table IX, it is seen that the largest vibrational dependence of the quadrupole coupling constant clearly arises from the large amplitude inversion mode, as expected. The present work completes the knowledge of the quadrupole coupling of the four fundamentals of ammonia

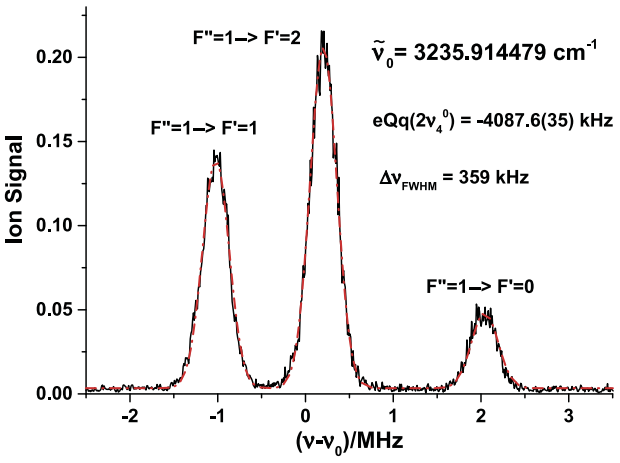

FIG. 14. High resolution spectra (as relative signal proportional to absorption) with resolved hyperfine structure for the ($J_K = 1_0$, $v_4 = 2$, l = 0, s, A_2^+) ← ($J_K = 0_0$, G.S., a, A_2^-) transition. The full line (black) gives the measured spectrum obtained from an average of 14 single scans and the dashed line (red) represents a fit of the hyperfine splitting according to Equations (19) and (20) to the experimental data resulting in three Gaussian lines with a common Doppler width ($\Delta\nu_{FWHM}$) of 359(5) kHz. A quadrupole coupling constant $eQq(2\nu_4^{l=0}, s) = -4087.6(35)$ kHz is derived, where the digits in parentheses represent the uncertainty of the fit (as 1σ in units of the last digits).

by adding the values for ν_1, ν_3 and provides also new values for the overtone $2\nu_4^0$ and $2\nu_4^{\pm 2}$, while for this latter mode, the value for the fundamental had been studied previously.[127] The quadrupole coupling constants for these excited levels differ only slightly from the ground state. Here, it is found for $2\nu_4$ that the coupling constant for the antisymmetric level is larger than for the corresponding symmetric level similar to ν_4, but different from the excited ν_2 levels. It should be clear that the coupling constants quoted are only effective spectroscopic constants.

VII. CONCLUSION

In the present work, we have demonstrated that it is possible to achieve substantial (about 80% per step) population transfer and parity selection in the final rotationally excited state by a sequential two step process, absorption followed by stimulated emission, for the spectroscopically simple prototypical molecule NH_3. The parity selection in this case starts from a thermal mixture of parity levels at low temperature. There is no substantial effect of collisions or other perturbations visible in this parity selection in our experiment. The fundamental setup uses single mode cw-OPOs with high power (up to 1.5 W), high frequency accuracy and stability, and bandwidth of 100 kHz or better. The REMPI detection of the prepared state achieves very high sensitivity.

One application of the present experiment is the measurement of the spectra of the ν_1 (symmetric NH_3 stretching) fundamental, the ν_3 (degenerate NH_3 stretching) fundamental, and the $2\nu_4$ (degenerate bending) overtone with hyperfine resolution, providing the ^{14}N quadrupole coupling constants, which were not previously known for these vibrational levels. With the present results and the previously known quadrupole coupling constants for other vibrational fundamentals, the set of coupling constants is now fairly complete for all vibrational fundamentals of $^{14}NH_3$.

The second important application of the present work concerns the proof of principle for future experiments on parity selection and the sensitive detection of a possible time evolution of parity due to parity violation in chiral molecules. From the flight times in the 1.3 ms range for the molecules in a molecular beam and the sensitivity achieved one can estimate that parity violating energy differences on the order of $(hc)10^{-12}$ cm^{-1} (corresponding to about 100 aeV or $\Delta_{pv}H_0^{\ominus}$ of 10^{-11} J mol^{-1}) should result in a detectable signal. Such values have been found theoretically in chiral molecules with nuclei not heavier than sulfur and chlorine,[8,44,47,48,138–140] which would be of great advantage for future fundamental theoretical analysis of such experimental results, once available, as discussed in Ref. 8. Flight and evolution times can be increased without change of the setup by using heavier seeding gases like krypton and xenon. One could, of course, consider also experiments on suitable chiral molecules involving heavier nuclei (see reviews of Refs. 8 and 46–49), which should result in very large and easily detectable signals in the present approach. However, limitations arise clearly for the selection of appropriate molecules, for which the present approach has severe requirements concerning sufficiently small spectroscopic complexity and the possibility of finding intermediate states with well defined parity in the process of parity selection. Selecting such molecules by theoretical prediction, synthesis, and subsequent spectroscopic analysis is an important next step in such a project, after the basic experimental procedure has been proven in the present work.

The present experimental approach and setup could also be used, in principle, for more conventional selection experiments, such as quantum state selection of different conformers of molecules showing tunneling switching,[141] or for the study of slow tunneling in chiral molecules at very high frequency resolution with possible applications to the study of molecular flux densities,[142] to mention just two selected examples of current interest. Also reaction dynamics with resolution of nuclear hyperfine effects could be studied with such a setup, as so far only few hyperfine resolved reaction dynamics are available.[143] Finally, spectroscopic results on rovibrational transitions with hyperfine resolution as obtainable with the present technique may have applications in an astrophysical context.[144,145]

ACKNOWLEDGMENTS

Early developments towards the present experiment in our group profited from contributions of Fatih Ünlüh, and help from and discussions with him, and S. Albert, I. Bolotova, Z. Chen, C. Fabri, L. Horný, and R. Prentner are gratefully acknowledged. We thank Andres Laso and Eduard Peyer for very important technical support. Our work is supported financially by the ETH Zürich and the Schweizerischer Nationalfonds and an advanced grant from the European Research Council. This work has, in particular, received funding under the European Unions's Seventh Framework program (No. FP7/2007-2013) ERC Grant No. 290925. It is also connected to the COST project MOLIM.

[1]J. H. van't Hoff, *La Chimie Dans L'Espace* (P.M. Bazendijk, Rotterdam, 1887), reprinted with commentary in "Sur la dissymétrie moléculaire," edited by C. Bourgeois, Coll. Epistème Paris 1986, pp. 109-222.
[2]*Louis Pasteur, J. H. van't Hoff, A. Werner, Sur la Dissymmétrie Moléculaire*, edited by C. Bourgois (Collection Epistème, Dole, 1986).
[3]J. H. van't Hoff, *Vorlesungen über Theoretische und Physikalische Chemie* (F. Vieweg Verlag, Braunschweig, 1899), Band 2.
[4]F. Hund, Z. Phys. **43**, 788 (1927).
[5]F. Hund, Z. Phys. **43**, 805 (1927).
[6]V. Prelog, "Chirality in chemistry," in *Les prix Nobel en 1975*, Nobel Lectures, 1975.
[7]M. Quack, Eur. Rev. **22**, S50 (2014).
[8]M. Quack, "Fundamental symmetries and symmetry violations from high resolution spectroscopy," in *Handbook of High Resolution Spectroscopy*, edited by M. Quack and F. Merkt (Wiley, Chichester, New York, 2011), Vol. 1, Chap. 18, pp. 659–722.
[9]S. F. Mason, *Chemical Evolution: Origins of the Elements, Molecules and Living Systems* (Clarendon Press, Oxford, 1991).
[10]P. Frank, W. Bonner, and R. N. Zare, "On the one hand but not on the other: The challenge of the origin and survival of homochirality in prebiotic chemistry," in *Chemistry for the 21st Century*, edited by E. Keinan and I. Schechter (Wiley-VCH, Weinheim, 2001), Chap. 11, pp. 175–208.
[11]M. Quack, Angew. Chem., Int. Ed. **41**, 4618 (2002).
[12]J. Jortner, Philos. Trans. R. Soc., B **361**, 1877 (2006).
[13]M. Quack, Adv. Chem. Phys. **157**, 249 (2014).
[14]T. Lee and C. Yang, Phys. Rev. **104**, 254 (1956).
[15]C. Wu, E. Ambler, R. Hayward, D. Hoppes, and R. Hudson, Phys. Rev. **105**, 1413 (1957).
[16]J. I. Friedman and V. L. Telegdi, Phys. Rev. **105**, 1681 (1957).

[17]R. L. Garwin, L. M. Lederman, and M. Weinrich, Phys. Rev. **105**, 1415 (1957).
[18]S. L. Glashow, Nucl. Phys. **22**, 579 (1961).
[19]S. Weinberg, Phys. Rev. Lett. **19**, 1264 (1967).
[20]A. Salam, "Weak and electromagnetic interactions," in *Elementary Particle Theory: Relativistic Groups and Analyticity. Proceedings of the 8th Nobel Symposium Held May 19-25, 1968 at Aspenäsgården, Lerum, in the County of Älvsborg, Sweden*, edited by N. Svartholm (Almkvist & Wiksell, Stockholm, 1968), pp. 367–377.
[21]M. J. G. Veltman, Rev. Mod. Phys. **72**, 341 (2000).
[22]G. 't Hooft, Rev. Mod. Phys. **72**, 333 (2000).
[23]Y. Yamagata, J. Theor. Biol. **11**, 495 (1966).
[24]D. W. Rein, J. Mol. Evol. **4**, 15 (1974).
[25]V. S. Letokhov, Phys. Lett. A **53**, 275 (1975).
[26]R. A. Hegström, D. W. Rein, and P. G. H. Sandars, J. Chem. Phys. **73**, 2329 (1980).
[27]S. F. Mason and G. E. Tranter, Mol. Phys. **53**, 1091 (1984).
[28]M. A. Bouchiat and C. Bouchiat, J. Phys. **35**, 899 (1974).
[29]M. A. Bouchiat and C. Bouchiat, J. Phys. **36**, 493 (1975).
[30]R. Conti, P. Bucksbaum, S. Chu, E. Commins, and L. Hunter, Phys. Rev. Lett. **42**, 343 (1979).
[31]S. C. Bennett and C. E. Wieman, Phys. Rev. Lett. **82**, 2484 (1999).
[32]V. M. Shabaev, K. Pachucki, I. Tupitsyn, and V. A. Yerokhin, Phys. Rev. Lett. **94**, 213002 (2005).
[33]K. Tsigutkin, D. Dounas-Frazer, A. Family, J. E. Stalnaker, V. V. Yashchuk, and D. Budker, Phys. Rev. Lett. **103**, 071601 (2009).
[34]A. Bakasov, T. K. Ha, and M. Quack, "*Ab initio* calculation of molecular energies including parity violating interactions," in *Chemical Evolution, Physics of the Origin and Evolution of Life, Proceedings of the 4th Trieste Conference (1995)*, edited by J. Chela-Flores and F. Raulin (Kluwer Academic Publishers, Dordrecht, 1996), pp. 287–296.
[35]P. Lazzeretti and R. Zanasi, Chem. Phys. Lett. **279**, 349 (1997).
[36]A. Bakasov, T. K. Ha, and M. Quack, J. Chem. Phys. **109**, 7263 (1998).
[37]A. Bakasov and M. Quack, Chem. Phys. Lett. **303**, 547 (1999).
[38]J. K. Laerdahl and P. Schwerdtfeger, Phys. Rev. A **60**, 4439 (1999).
[39]R. Berger and M. Quack, J. Chem. Phys. **112**, 3148 (2000).
[40]M. Quack and J. Stohner, Phys. Rev. Lett. **84**, 3807 (2000).
[41]J. K. Laerdahl, P. Schwerdtfeger, and H. M. Quiney, Phys. Rev. Lett. **84**, 3811 (2000).
[42]M. Quack and J. Stohner, J. Chem. Phys. **119**, 11228 (2003).
[43]A. C. Hennum, T. Helgaker, and W. Klopper, Chem. Phys. Lett. **354**, 274 (2002).
[44]L. Horný and M. Quack, Mol. Phys. **113**, 1768 (2015).
[45]M. Quack and J. Stohner, Chirality **13**, 745 (2001).
[46]R. Berger, "Parity-violation effects in molecules," in *Relativistic Electronic Structure Theory, Part 2*, edited by P. Schwerdtfeger (Elsevier, Amsterdam, 2004), Chap. 4, pp. 188–288.
[47]M. Quack and J. Stohner, Chimia **59**, 530 (2005); Erratum, **59**, 712 (2005).
[48]M. Quack, J. Stohner, and M. Willeke, Annu. Rev. Phys. Chem. **59**, 741 (2008).
[49]B. Darquié, C. Stoeffler, A. Shelkovnikov, C. Daussy, A. Amy-Klein, C. Chardonnet, S. Zrig, L. Guy, J. Crassous, P. Soulard, P. Asselin, T. R. Huet, P. Schwerdtfeger, R. Bast, and T. Saue, Chirality **22**, 870 (2010).
[50]M. Quack, "Frontiers in spectroscopy," Faraday Discuss. **150**, 533–565 (2011).
[51]O. N. Kompanets, A. R. Kukudzhanov, V. S. Letokhov, and L. L. Gervits, Opt. Commun. **19**, 414 (1972).
[52]E. Arimondo, P. Glorieux, and T. Oka, Opt. Commun. **23**, 369 (1977).
[53]R. A. Harris and L. Stodolsky, Phys. Lett. B **78**, 313 (1978).
[54]M. Quack, Chem. Phys. Lett. **132**, 147 (1986).
[55]M. Quack, Angew. Chem., Int. Ed. Engl. **28**, 571 (1989); Angew. Chem. **101**, 588-604 (1989).
[56]M. J. M. Pepper, I. Shavitt, P. von Ragué Schleyer, M. N. Glukhovtsev, R. Janoschek, and M. Quack, J. Comput. Chem. **16**, 207 (1995).
[57]A. Bauder, A. Beil, D. Luckhaus, F. Müller, and M. Quack, J. Chem. Phys. **106**, 7558 (1997).
[58]C. Daussy, T. Marrel, A. Amy-Klein, C. Nguyen, C. Borde, and C. Chardonnet, Phys. Rev. Lett. **83**, 1554 (1999).
[59]M. Schnell and J. Küpper, Faraday Discuss. **150**, 33 (2011).
[60]S. K. Tokunaga, C. Stoeffler, F. Auguste, A. Shelkovnikov, C. Daussy, A. Amy-Klein, C. Chardonnet, and B. Darquié, Mol. Phys. **111**, 2363 (2013).
[61]P. Dietiker, E. Miloglyadov, M. Quack, A. Schneider, and G. Seyfang, "Two photon IR-laser induced population transfer in NH_3: First steps to measure parity violation in chiral molecules," in *Proceedings of the 19th Symposium on Atomic, Cluster and Surface Physics 2014 (SASP 2014), Obergurgl, Austria, 8 to 14 February 2014*, edited by D. Stock, R. Wester, and P. Scheier (Innsbruck University Press (IUP), Innsbruck, 2014), pp. 226–229.
[62]M. Gottselig and M. Quack, J. Chem. Phys. **123**, 84305 (2005).
[63]M. Quack and M. Willeke, J. Phys. Chem. A **110**, 3338 (2006).
[64]M. Hippler and M. Quack, J. Chem. Phys. **104**, 7426 (1996).
[65]M. Hippler, E. Miloglyadov, M. Quack, and G. Seyfang, "Mass and isotope selective infrared spectroscopy," in *Handbook of High Resolution Spectroscopy*, edited by M. Quack and F. Merkt (Wiley, Chichester, New York, 2011), Vol. 2, Chap. 28, pp. 1069–1118.
[66]S. Gerstenkorn and P. Luc, *Atlas du Spectre D′ absorption de la Molécule D′ iode 14800 - 20000* cm^{-1} (Éditions du CNRS, 1978).
[67]H. C. W. Beijerinck and N. F. Verster, Physica C **111**, 327 (1981).
[68]A. F. Linskens, N. Dam, B. Sartakov, and J. Reuss, Chem. Phys. Lett. **248**, 244 (1996).
[69]V. Špirko, J. M. R. Stone, and D. Papousek, J. Mol. Spectrosc. **60**, 159 (1976).
[70]R. Marquardt, K. Sagui, J. Zheng, W. Thiel, D. Luckhaus, S. Yurchenko, - F. Mariotti, and M. Quack, J. Phys. Chem. A **117**, 7502 (2013).
[71]R. Marquardt, K. Sagui, W. Klopper, and M. Quack, J. Phys. Chem. B **109**, 8439 (2005).
[72]H. C. Longuet-Higgins, Mol. Phys. **6**, 445 (1963).
[73]M. Quack, Mol. Phys. **34**, 477 (1977).
[74]E. R. Cohen, T. Cvitas, J. G. Frey, B. Holmström, K. Kuchitsu, R. Marquardt, I. Mills, F. Pavese, M. Quack, J. Stohner, H. L. Strauss, M. Takami, and A. J. Thor, *Quantities, Units and Symbols in Physical Chemistry*, 3rd ed. (IUPAC and Royal Society of Chemistry, RSC Publishing, Cambridge, 2011), third corrected printing.
[75]T. Oka, "Orders of magnitude and symmetry in molecular spectroscopy," in *Handbook of High Resolution Spectroscopy*, edited by M. Quack and F. Merkt (Wiley, Chichester, New York, 2011), Vol. 1, Chap. 17, pp. 633–658.
[76]M. Schnell, "Group theory for high-resolution spectroscopy of nonrigid molecules," in *Handbook of High Resolution Spectroscopy*, edited by M. Quack and F. Merkt (Wiley, Chichester, New York, 2011), Vol. 1, Chap. 16, pp. 607–632.
[77]M. Snels, L. Fusina, H. Hollenstein, and M. Quack, Mol. Phys. **98**, 837 (2000).
[78]M. Snels, H. Hollenstein, and M. Quack, J. Chem. Phys. **125**, 194319 (2006).
[79]A. Amrein, M. Quack, and U. Schmitt, J. Phys. Chem. **92**, 5455 (1988).
[80]M. Hepp, G. Winnewisser, and K. M. T. Yamada, J. Mol. Spectrosc. **153**, 376 (1992).
[81]B. D. Kay and A. J. Grimley, Chem. Phys. Lett. **127**, 303 (1986).
[82]A. Bach, J. M. Hutchison, R. J. Holiday, and F. F. Crim, J. Chem. Phys. **116**, 4955 (2002).
[83]C. M. Tanner, M. Quack, and D. Schmidiger, J. Phys. Chem. A **117**, 10105 (2013).
[84]I. Kleiner, L. R. Brown, G. Tarrago, Q.-L. Kou, N. Piqué, G. Guelachvili, V. Dana, and J.-Y. Mandin, J. Mol. Spectrosc. **193**, 46 (1999).
[85]A. Douglas and J. M. Hollas, Can. J. Phys. **39**, 479 (1961).
[86]A. E. Douglas, Discuss. Faraday Soc. **35**, 158 (1963).
[87]J. H. Glownia, S. J. Riley, S. D. Colson, and G. C. Nieman, J. Chem. Phys. **72**, 5998 (1989).
[88]M. N. R. Ashfold, R. N. Dixon, and R. J. Stickland, Chem. Phys. **88**, 463 (1984).
[89]W. A. Conaway, R. J. S. Morrison, and R. N. Zare, Chem. Phys. Lett. **113**, 429 (1985).
[90]J. M. Allen, M. N. R. Ashfold, R. J. Stickland, and C. M. Western, Mol. Phys. **74**, 49 (1991).
[91]M. Nolde, K.-M. Weitzel, and C. M. Western, Phys. Chem. Chem. Phys. **7**, 1527 (2005).
[92]M. N. R. Ashfold, G. A. King, M. G. D. Nix, and A. A. Oliver, "High-resolution photofragment translational spectroscopy using Rydberg tagging methods," in *Handbook of High Resolution Spectroscopy*, edited by M. Quack and F. Merkt (Wiley, Chichester, New York), Vol. 3, Chap. 15, pp. 1859–1883.
[93]C. Placzek and E. Teller, Z. Phys. **81**, 209 (1933).
[94]K. Chen and E. S. Yeung, J. Chem. Phys. **69**, 43 (1978).
[95]F. Merkt and M. Quack, "Molecular quantum mechanics and molecular spectra, molecular symmetry, and interaction of matter with radiation," in *Handbook of High-Resolution Spectroscopy*, edited by M. Quack and F. Merkt (Wiley, Chichester, New York, 2011), Vol. 1, Chap. 1, pp. 1–55 (see also preface to this handbook).

[96]W. Gordy and R. L. Cook, *Microwave Molecular Spectra*, 1st ed. (John Wiley, New York, 1984).
[97]H. W. Kroto, *Molecular Rotation Spectra* (Wiley, London, New York, Toronto, 1979).
[98]R. N. Zare, *Angular Momentum*, 1st ed. (John Wiley, New York, 1988).
[99]G. Cazzoli, L. Dore, and C. Puzzarini, Astron. Astrophys. **507**, 1707 (2009).
[100]M. Quack, J. Chem. Phys. **69**, 1282 (1978).
[101]R. Loudon, *The Quantum Theory of Light*, 1st ed. (Clarendon Press, Oxford, 1973).
[102]K. Bergmann, H. Theuer, and B. W. Shore, Rev. Mod. Phys. **70**, 1003 (1998).
[103]W. Dong, N. Mukherjee, and R. N. Zare, J. Chem. Phys. **139**, 074204 (2013).
[104]C. Liedenbaum, S. Stolte, and J. Reuss, Infrared Phys. **29**, 397 (1989).
[105]C. Liedenbaum, S. Stolte, and J. Reuss, Phys. Rep. **178**, 1 (1989).
[106]U. Gaubatz, P. Rudeki, S. Schieman, and K. Bergmann, J. Chem. Phys. **92**, 5363 (1990).
[107]M. P. Fewell, B. W. Shore, and K. Bergmann, Aust. J. Phys. **50**, 281 (1997).
[108]W. Demtöder, *Laser Spectroscopy I: Basic Principles*, 5th ed. (Springer, Berlin, Heidelberg, 2014).
[109]W. E. Good, Phys. Rev. **70**, 213 (1946).
[110]D. K. Coles and W. E. Good, Phys. Rev. **70**, 979 (1946).
[111]G. R. Gunther-Mohr, R. L. White, A. L. Schawlow, W. Good, and D. K. Coles, Phys. Rev. **94**, 1184 (1954).
[112]G. R. Gunther-Mohr, C. H. Townes, and J. H. Van Vleck, Phys. Rev. **94**, 1191 (1954).
[113]J. P. Gordon, Phys. Rev. **99**, 1253 (1955).
[114]S. G. Kukolich, Phys. Rev. **138**, 1322 (1965).
[115]S. G. Kukolich, Phys. Rev. **156**, 83 (1967).
[116]S. G. Kukolich and S. C. Wofsy, J. Chem. Phys. **52**, 5477 (1970).
[117]J. T. Hougen, J. Chem. Phys. **57**, 4207 (1972).
[118]M. D. Marshall and J. S. Muenter, J. Mol. Spectrosc. **85**, 322 (1981).
[119]W. Hüttner and W. Majer, Mol. Phys. **52**, 631 (1984).
[120]S. P. Belov, S. Urban, and G. Winnewisser, J. Mol. Spectrosc. **189**, 1 (1998).
[121]M. Ouhayoun, C. J. Bordé, and J. Bordé, Mol. Phys. **33**, 597 (1977).
[122]G. Magerl, W. Schupita, J. M. Frye, W. A. Kreiner, and T. Oka, J. Mol. Spectrosc. **107**, 72 (1984).
[123]H. Fichoux, M. Khelkhal, E. Rusinek, J. Legrand, F. Herlemont, and S. Urban, J. Mol. Spectrosc. **192**, 169 (1998).
[124]S. Urban, F. Herlemont, M. Khelkhal, H. Fichoux, and J. Legrand, J. Mol. Spectrosc. **200**, 280 (2000).
[125]C. Lemarchand, M. Triki, B. Darquié, C. J. Bordé, C. Chardonnet, and C. Daussy, New J. Phys. **13**, 073028 (2011).
[126]W. H. Weber and R. W. Terhune, J. Chem. Phys. **78**, 6422 (1983).
[127]W. H. Weber, J. Opt. Soc. Am. B **2**, 829 (1985).
[128]P. Grigolini and R. Moccia, J. Chem. Phys. **57**, 1369 (1972).
[129]V. Špirko, Mol. Phys. **38**, 1761 (1979).
[130]F. Michelot, Mol. Phys. **45**, 949 (1982).
[131]F. Michelot, Mol. Phys. **45**, 971 (1982).
[132]M. R. Aliev and J. T. Hougen, J. Mol. Spectrosc. **106**, 110 (1984).
[133]P. W. Fowler and V. Špirko, J. Chem. Soc., Faraday Trans. **86**, 1991 (1990).
[134]J. Oddershede, I. Paidarová, and V. Špirko, J. Mol. Spectrosc. **152**, 342 (1992).
[135]P. Piecuch, V. Špirko, and J. Paldus, J. Chem. Phys. **105**, 11068 (1996).
[136]C. Puzzarini, Theor. Chem. Acc. **121**, 1 (2008).
[137]T. K. Ha, Chem. Phys. Lett. **107**, 117 (1984).
[138]R. Berger, M. Gottselig, M. Quack, and M. Willeke, Angew. Chem., Int. Ed. **40**, 4195 (2001); Angew. Chem. **113**, 4342-4345 (2001).
[139]C. Fàbri, L. Horný, and M. Quack, in Proceedings QAMTS 2015, paper P6; C. Fabri, R. Marquardt, and M. Quack, *ibid.*, paper L42; C. Fabri, L. Horny, and M. Quack, ChemPhysChem **16**, 3584 (2015); R. Prentner, M. Quack, J. Stohner, and M. Willeke, "Wavepacket dynamics of the axially chiral molecule Cl–O–O–Cl under coherent radiative excitation and including electroweak parity violation," J. Phys. Chem. A (published online).
[140]S. Albert, I. Bolotova, Z. Chen, C. Fàbri, L. Hornỳ, M. Quack, G. Seyfang, and D. Zindel, in Proceedings QAMTS 2015, paper P10.
[141]S. Albert, P. Lerch, R. Prentner, and M. Quack, Angew. Chem., Int. Ed. **52**, 346 (2013).
[142]T. Grohmann, J. Manz, and A. Schild, Mol. Phys. **111**, 2251 (2011).
[143]Y. B. He, J. Pochert, M. Quack, R. Ranz, and G. Seyfang, Faraday Discuss. **102**, 275 (1995).
[144]L. H. Coudert and R. Roueff, Astron. Astrophys. **449**, 855 (2006).
[145]C. M. Persson, M. Olberg, Å. Hjalmarson, M. Spaans, J. H. Black, U. Frisk, T. Liljeström, A. O. H. Olofsson, D. R. Poelman, and A. Sandqvist, Astron. Astrophys. **494**, 637 (2009).
[146]S. R. Langford, A. J. Orr-Ewing, R. A. Morgan, C. M. Western, M. N. R. Ashfold, A. Rijkenberg, C. A. Scheper, W. J. Buma, and C. A. de Lange, J. Chem. Phys. **108**, 6667 (1999).